



# LMC-driven Anisotropic Boosts in Stream–Subhalo Interactions

Arpit Arora<sup>1</sup> , Nicolás Garavito-Camargo<sup>2</sup> , Robyn E. Sanderson<sup>1,2</sup> , Emily C. Cunningham<sup>2,3,7</sup> , Andrew Wetzel<sup>4</sup> ,  
Nondh Panithanpaisal<sup>1,5,6</sup> , and Megan Barry<sup>4</sup>

<sup>1</sup>Department of Physics & Astronomy, University of Pennsylvania, 209 S. 33rd St., Philadelphia, PA 19104, USA; [arora125@sas.upenn.edu](mailto:arora125@sas.upenn.edu)

<sup>2</sup>Center for Computational Astrophysics, Flatiron Institute, 162 5th Ave., New York, NY 10010, USA

<sup>3</sup>Department of Physics & Astronomy, Columbia University, 550 West 120th St., New York, NY 10027, USA

<sup>4</sup>Department of Physics & Astronomy, University of California, Davis, Davis, CA 95616, USA

<sup>5</sup>Carnegie Observatories, 813 Santa Barbara St., Pasadena, CA 91101, USA

<sup>6</sup>TAPIR, California Institute of Technology, Pasadena, CA 91125, USA

Received 2023 September 27; revised 2024 August 16; accepted 2024 August 23; published 2024 October 17

## Abstract

Dark matter subhalos are predicted to perturb stellar streams; stream morphologies and dynamics can, therefore, constrain the mass distribution of subhalos. Using FIRE-2 simulations of Milky Way–mass galaxies, we demonstrate that the presence of an LMC analog significantly changes stream–subhalo encounter rates. The LMC analog brings in many subhalos, increasing encounter rates for streams near the massive satellite by 10%–40%. Additionally, the LMC analog displaces the host from its center of mass (inducing reflex motion), which causes a north–south asymmetry in the density and radial velocity distributions of subhalos. This asymmetry, combined with the presence of LMC-analog subhalos, causes encounter rates at the same distance to vary by 50%–70% across the sky, particularly in regions opposite the LMC analog. Furthermore, the LMC analog induces a density wake in the host’s dark matter halo, further boosting the encounter rates near the LMC analog. We also explore how stream orbital properties affect encounter rates, finding up to a 50% increase for streams moving retrograde to the LMC analog’s orbit in the opposite quadrant. Finally, we report the encounter rates for Milky Way streams within the context of our simulations, both with and without the presence of an LMC analog. The dependence of encounter rates on stream location, orbit, and their position relative to the LMC has important implications for where to search for streams with spurs and gaps in the Milky Way.

*Unified Astronomy Thesaurus concepts:* [Stellar streams \(2166\)](#); [Dark matter \(353\)](#); [Large Magellanic Cloud \(903\)](#)

## 1. Introduction

A promising indirect method to constrain the nature of dark matter (DM) is by measuring the mass function of dark subhalos. At these small scales, different DM models (that have yet to be ruled out observationally) have different predictions for the number of expected subhalos as a function of mass. For example, in the cold DM (CDM) paradigm, the predicted number of dark subhalos with a mass of about  $10^7 M_\odot$  for a galaxy like the Milky Way (MW) is approximately  $10^3$  subhalos, while in warm DM (WDM) models the expected number depends on the mass of the WDM particles and ranges from 10 to  $10^3$  dark subhalos (e.g., S. Y. Kim et al. 2018). In self-interacting DM models with velocity-dependent cross section and maximum transfer cross section of about  $3.5 \text{ cm}^2 \text{ g}^{-1}$ , we expect around 100 subhalos (e.g., M. Vogelsberger et al. 2012; V. H. Robles et al. 2019; E. O. Nadler et al. 2021). Thus, measuring the abundance of subhalos at mass scales below  $10^7 M_\odot$  would provide strong constraints between different DM models. A promising way to detect subhalos in the MW is by observing their signatures after they interact with cold substructures such as stellar streams (K. V. Johnston et al. 2002; D. Erkal & V. Belokurov 2015b; J. L. Sanders et al. 2016; J. Bovy et al. 2017; K. Malhan et al. 2021). The prime

example is the GD-1 stream, a long (10 kpc, approximately  $100^\circ$ ) and thin (20 pc) stream around the MW (C. J. Grillmair & O. Dionatos 2006). The density of the stream is not smooth, but rather shows several gaps in density, one overdensity, and stars orbiting with the stream above the main stream track, known as “the spur” (A. M. Price-Whelan & A. Bonaca 2018; K. Malhan et al. 2019). Detailed orbital modeling has constrained the mass of the perturber to be  $10^6$ – $10^8 M_\odot$ , possibly originating as a subhalo brought by the Sagittarius dwarf galaxy (A. Bonaca et al. 2019). However, the concentration of this perturber is marginally consistent with predictions for CDM subhalos (T. de Boer et al. 2020; N. Banik et al. 2021b, 2021a). These results have motivated searches for further observational evidence of stream–subhalo interactions across the MW’s halo.

Currently, there are about 100 known streams in the MW (C. Mateu 2023) located at different distances and in different regions of the sky, providing a unique opportunity to detect the signatures of dark subhalos across the galaxy. Surveys such as Gaia (Gaia Collaboration et al. 2016), DESI (C. DESI et al. 2016), H3 (C. Conroy et al. 2019), the Vera Rubin Observatory (Ž. Ivezić et al. 2019), WEAVE (G. Dalton et al. 2012), 4MOST (R. S. De Jong et al. 2019), and Subaru PFS (M. Takada et al. 2014), among others, will further observe streams all the way to the edge of the Galaxy and in external galaxies (S. Pearson et al. 2022; C. Aganze et al. 2023). The data from all of these surveys will provide a multidimensional view (kinematics and chemistry) of the stellar halo that will allow the detection and characterization of the morphology of stellar streams and, hence, the detection of low-mass, completely dark subhalos.

<sup>7</sup> NASA Hubble Fellow.

Assuming that more perturbed streams can be found, and with their perturbers constrained with dynamical modeling, obtaining constraints on the properties of the DM particle from these few perturbers requires interpreting their consistency with the population of subhalos predicted for each DM model. The usual practice currently is to assume that the DM subhalo population is isotropic (e.g., R. G. Carlberg 2009; J. H. Yoon et al. 2011; D. Erkal & V. Belokurov 2015a; J. Bovy 2016; J. L. Sanders et al. 2016). However, the MW’s distribution of satellite galaxies and subhalos is almost certainly *anisotropic* (e.g., E. O. Nadler et al. 2020; M. S. Pawlowski & P. Kroupa 2020; H. Li et al. 2021a; A. Savino et al. 2022). One of the main causes of this anisotropic distribution is the anisotropic accretion through filaments (N. I. Libeskind et al. 2011) and recent accretion of the Magellanic Clouds; here we will focus on the effect from these massive satellites, which are causing several disequilibria throughout the Galaxy (see, e.g., E. Vasiliev 2023 for a recent review). In short, the LMC brings its own subhalos distributed along the DM debris (e.g., A. J. Deason et al. 2015; A. R. Wetzel et al. 2015; L. V. Sales et al. 2017); displaces the host from its center of mass (COM; inducing reflex motion), causing a north–south asymmetry in the density and radial velocity distributions (e.g., D. Erkal et al. 2019; N. Garavito-Camargo et al. 2019; M. S. Petersen & J. Peñarrubia 2020); and induces a DM density wake in the host’s DM halo (N. Garavito-Camargo et al. 2019) and stellar halo (E. C. Cunningham et al. 2020; C. Conroy et al. 2021). As a result, streams located in different locations in the sky but at the same Galactocentric distance would experience different interaction rates with DM subhalos.

Recently, M. Barry et al. (2023) calculated the enhancement effect of LMC-mass satellites on several subhalo population metrics, including the number density and orbital flux. They found that the presence of an LMC-mass satellite enhances these population metrics by up to factors of 1.2–2. They also computed the spherically averaged subhalo encounter rates as a function of distance from the host center. However, within the MW, the encounter rates are subject to azimuthal variations due to the host’s response to the infalling satellite and the subhalos brought in by the LMC itself. In this paper, we quantify the effect of massive LMC-mass satellites on the subhalo–stream interaction in one of the systems that is most LMC-like in its orbit and mass ratios at first pericenter. By using the Latte suite of FIRE-2 simulations (A. R. Wetzel et al. 2016; A. Wetzel et al. 2023), we predict which regions in the halo would have higher subhalo–stream interactions. Our study provides a more detailed and context-specific analysis of the MW system, offering a complementary perspective to the broader picture painted by M. Barry et al. (2023).

The structure of this paper is as follows: In Section 2, we provide a detailed explanation of our choice of zoomed-in cosmological FIRE-2 simulations. We identify the closest MW–LMC analog in the FIRE-2 suite and establish the analytical models to compute stream–subhalo encounter rates. Additionally, we demonstrate how we inject both the real MW and synthetic streams and integrate their orbits to calculate encounter rates. In Section 3, we investigate the impact of infalling satellites and the MW’s response on encounter rates. We analyze key parameters influencing these rates, including the DM wake, collective response, and reflex motion. In Section 4, we present the computed encounter rates for both synthetic streams and the injected real MW streams. Statistical analysis is used to highlight key differences observed in the

encounter rates, which are dependent on stream properties and their local positions. Finally, in Section 5, we discuss the implications of our results in the context of the MW. Our conclusions are presented in Section 6.

## 2. Stream–Subhalo Encounters in Simulations

In this section, we detail our approach to studying the stream–subhalo encounter rates in simulations of MW-mass galaxies. We begin by explaining our choice of the simulations and the methodology for identifying the LMC analog. Next, we establish the galactocentric and stream-centric coordinate systems necessary for the analysis. We then outline our subhalo selection criteria and track the LMC-associated subhalos, examining their spatial distribution and assessing their “survival status,” i.e., whether they are bound to or disrupted by the LMC analog or the MW.

Furthermore, we introduce our analytical model, outlining the assumptions used to compute the stream–subhalo encounter rates. This involves integrating representative orbits for a suite of both synthetic and real MW streams.

### 2.1. Simulations

We select two cosmological zoomed-in baryonic simulations of MW-mass galaxies from the Latte suite (A. Wetzel et al. 2023) of the Feedback In Realistic Environments (FIRE) project.<sup>8</sup> These simulations are run with the FIRE-2 physics model (P. F. Hopkins et al. 2018) using the GIZMO code (P. F. Hopkins 2015), which utilizes a TREE+PM solver for gravity and a Lagrangian meshless finite mass solver for hydrodynamics with adaptive spatial resolution. The FIRE-2 model implements star formation and stellar feedback parameters from the Starburst99 stellar evolution models (C. Leitherer et al. 1999) in the  $\Lambda$ CDM cosmology from Planck (P. Collaboration et al. 2016). A detailed description of the FIRE-2 project can be found in P. F. Hopkins et al. (2018), and a description of the Latte suite of MW-mass systems specifically can be found in A. R. Wetzel et al. (2016). D. Horta et al. (2023) made predictions for observable properties of the LMC-analog accretion events in the Latte MW analogs, while N. Panithanpaisal et al. (2021) studied the mass distribution of massive stellar streams and their progenitors. J. Samuel et al. (2020) examined the radial velocity distribution of satellites around isolated and paired MW–M31 analogs and showed that the central disk tidally destroys satellites, altering their radial profile. J. Samuel et al. (2021) showed that spatially thin MW-like planes of satellites can exist in cosmological simulation and the presence of an LMC analog increases the probability of such planes. M. Barry et al. (2023) did a statistical study of spherically averaged subhalo number density and estimated a boost of 1.2–2 due to the LMC analogs. They also estimated that a stream like GD-1 (C. J. Grillmair & O. Dionatos 2006) can have roughly five to six encounters per gigayear.

We select two galaxies labeled m12i and m12b for our analysis. Both are similar to the MW in stellar and gas mass content and their DM mass and density profiles at the present day (P. F. Hopkins et al. 2018; S. Garrison-Kimmel et al. 2018; R. E. Sanderson et al. 2020). Each DM halo has a total mass of about  $1. \times 10^{12} M_{\odot}$ , and each simulation uses an initial particle

<sup>8</sup> <http://fire.northwestern.edu/latte>

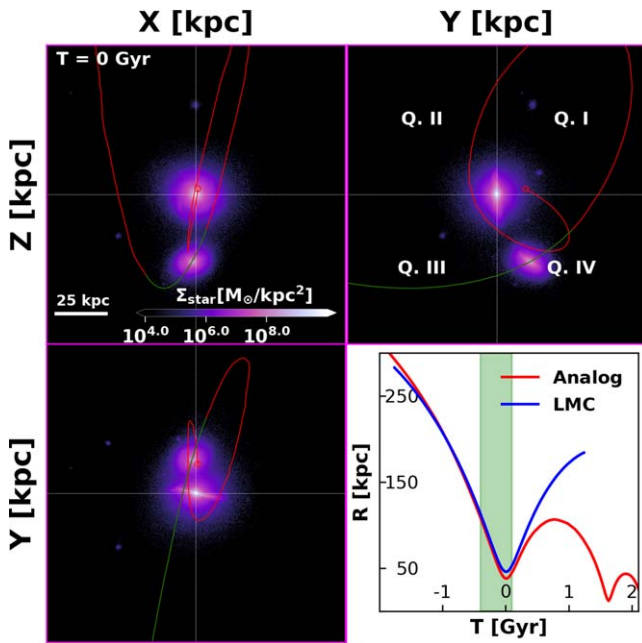


**Figure 1.** Trajectory of the LMC analog (red/green) in the rotated axis galactocentric coordinates from FIRE-2 simulation of an MW-mass galaxy labeled m12b with stellar surface density in the background at  $T = 0$  Gyr (first pericenter). Quadrant labels based on Table 2 are marked in the  $Y$ - $Z$  plane. Bottom right: the distance from the galactic center as a function of time for the FIRE analog (red/green), compared to the MW-LMC simulation 3 from N. Garavito-Camargo et al. (2019; blue). The green sections of the trajectories indicate the periods over which we compute encounter rates.

mass of  $m_b = 7100 M_\odot$  for stars and gas and a DM particle mass  $m_{\text{DM}} = 35,000 M_\odot$ . m12b includes a massive satellite analogous to the LMC in the MW with its first pericentric passage about 5 Gyr before the present day, while m12i has a relatively quiescent history with no major mergers for the past 8 Gyr and is used as our “control” system.

We identify the LMC analog in m12b based on the similarity of its orbit around first pericenter (Figure 1) and on the similar merger mass ratio of about 1:8 at pericenter (Table 1). The orbit has  $d_{\text{peri}} = 37.9$  kpc and  $v_{\text{tot}} \approx 350$  km s $^{-1}$ , comparable to the values of  $d_{\text{peri}} = 49$  kpc and  $v_{\text{tot}} = 350$  km s $^{-1}$  estimated for the LMC (N. Kallivayalil et al. 2006). Following A. Arora et al. (2022), we define the total mass ratio (TMR) to be the mass of the host galaxy divided by the mass of the satellite at  $T_{\text{peri}}$  and the pericenter mass ratio (PMR) to be the mass of the MW enclosed within  $d_{\text{peri}}$  divided by the mass brought in by the satellite within  $d_{\text{peri}}$  of the center of the satellite. The LMC analog has a TMR of 7.3, while the estimated TMR for the LMC is about  $\sim 4$ –15, assuming an MW mass of  $(1$ – $1.5) \times 10^{12} M_\odot$  and an LMC mass of  $(1$ – $2.5) \times 10^{11} M_\odot$  (e.g., J. Penarrubia et al. 2016; E. Vasiliev et al. 2021).

The main difference between our analog and the LMC, based on the models in N. Garavito-Camargo et al. (2019), is the plane of the satellite’s orbit relative to the host disk and that its first pericentric passage occurred about 5 Gyr before the present day. In our simulation, the LMC analog’s orbit is inclined at  $107^\circ$  oriented with respect to the disk plane. However, we do not expect this difference to significantly impact our conclusions. This is because we are interested in computing subhalo–stream interactions and determining their rates in different halo quadrants relative to the merger trajectory. Moreover, since the orientation of the LMC orbit is not very well constrained owing

to uncertainties in measured positions and proper motion and in the MW-mass models (P. J. McMillan 2016; G. Pietrzynski et al. 2019), our simulation with a slightly differently oriented LMC analog provides a plausible scenario. The torque from the disk could affect the orientation and shape of the streams, but the effect is expected to be minor. In fact, a number of studies have investigated the effect of the disk’s torque on the shape of tidal streams. For example, D. R. Law et al. (2005) found that the disk torque can significantly affect the orientation and shape of streams for nearly coplanar orbits, while for more inclined orbits the effect is much weaker. On the other hand, S. Kazantzidis et al. (2008) argued that the disk torque is generally not important for the formation of streams, since the subhalo’s motion in the host halo is dominated by the overall potential rather than the disk torque. I. B. Santistevan et al. (2024) showed that orbits of satellites in idealized host potentials are completely insensitive to host disk orientation. Furthermore, S. Garrison-Kimmel et al. (2017) showed that tidal disruption of subhalos remains largely unaffected by the geometry of the host disk. Therefore, while the effect of the disk torque on the shape of streams is still debated and likely depends on various factors such as the orbital parameters and the properties of the host and subhalo, it is generally believed to be small for orbits that are not nearly coplanar with the host disk.

The first pericenter passage of the LMC analog in m12b occurs at a look-back time of about 5 Gyr (Table 1), so we define the time  $T$  relative to it such that  $T_{\text{peri}} = 0$  Gyr. The most massive perturber in m12i reaches the pericenter around the same time and is nearly an order of magnitude less massive relative to its host at the pericenter than the LMC analog we identify in m12b. The age of our host galaxies at pericenter is thus less than the current age of the MW; however, given that the majority of star formation has slowed down by about 7 Gyr in both m12b and m12i (P. F. Hopkins et al. 2018) and the total mass of each halo is close to the MW at the time of the merger, we expect our simulations to be analogous to the real MW even though they are slightly younger than the MW at satellite pericenter. Table 1 summarizes the characteristics of the LMC analog in m12b and the equivalent most massive satellite in m12i at  $T_{\text{peri}} = 0$  Gyr.

M. Barry et al. (2023) [stop]showed that the presence of an LMC analog can boost the subhalo number density by a factor of 1.2–2. They identified four LMC analogs in simulations m12b, m12f, m12w, and m12c from the Latte suite of FIRE-2 simulations, approximating properties when the analogs approach within 50 kpc of the center and not their actual pericentric distances. This method provides greater statistical accuracy when evaluating the contribution of the LMC analogs to the subhalo population, but not necessarily to their phase-space distribution. Our focus here encompasses a global perspective that also considers the effects of the MW response to the infalling satellites, which is dependent on the satellite’s orbit, actual pericenter distance, mass, and velocity. The LMC-analog orbit in m12f is similar to the expected LMC orbit, but the infalling satellite is only half as massive, with a TMR of about 16 (A. Arora et al. 2022). Consequently, the host’s response to the LMC analog in m12f is significantly weaker.

Moving on to m12w and m12c, both simulations feature satellites similar in mass to the LMC. However, m12w stands out owing to its highly eccentric, fast-moving orbit, resulting in a very radial merger with its first pericenter at 8 kpc and eventual complete tidal disruption of the satellite. It is almost 6.5 Gyr

**Table 1**  
Properties of the Most Massive Mergers in m12b (LMC Analog) and m12i

Simulation	$T_{\text{peri}}$ (Gyr)	Redshift	$M_{*,\text{host}}$ ( $\times 10^{10} M_{\odot}$ )	$d_{\text{peri}}$ (kpc)	TMR	PMR	$v_{\text{rad}}$ ( $\text{km s}^{-1}$ )	$v_{\text{tan}}$ ( $\text{km s}^{-1}$ )
m12i	8.05	0.60	3.8	29.53	45.5	14.05	−13.4	290.2
m12b	8.81	0.49	6.3	37.9	8	3	−9.7	349.2

**Note.**  $T_{\text{peri}}$ : time of closest approach (“pericenter”) between the main galaxy and the satellite ( $T = 0$  Gyr). All properties are evaluated at  $T_{\text{peri}}$ .  $M_{*,\text{host}}$ : stellar mass of the halo.  $d_{\text{peri}}$ : pericenter distance between the satellite and the main galaxy. TMR: total mass ratio of the MW and the satellite,  $M_{\text{main}}/M_{\text{sat}}$ . PMR: pericenter mass ratio,  $M_{\text{main}}(<d_{\text{peri}})/M_{\text{sat}}(<d_{\text{peri}} \text{ from sat})$ .  $v_{\text{rad}}$ ,  $v_{\text{tan}}$ : radial and tangential velocities of the satellite with respect to the MW. Parameter  $v_{\text{rad}}$  is nonzero owing to finite time resolution between snapshots around the pericentric passage.

before the present day (1.5 Gyr earlier in comparison to m12b). This makes it highly unreliable for predictions. In contrast, the LMC analog in m12c is closest to the present day but follows an orbit completely within the disk plane, with the actual first pericenter occurring at 18 kpc. This particular orbit is not expected to induce a north–south asymmetry. Selecting an arbitrary pericenter at 50 kpc would not accurately represent halo deformations. For the sake of completeness, we have included our encounter rate calculation for m12c in Appendix C.

## 2.2. Coordinates and Frames for Analysis

The MW–LMC system we consider involves two galaxies orbiting around their common COM, which is moving with relatively constant velocity through space in a cosmological simulation box. The frame centered on and moving with the system COM is thus an inertial frame (modulo interactions with the next most massive satellite galaxy of the MW). We will refer to this as the system frame, marked by primed quantities, related to the one in which the simulation is run (the “simulation box frame”).

From our perspective in the MW’s disk, however, the Sun orbits the center of the MW (the local minimum in the potential and maximum in density), and we commonly use a coordinate system centered on and moving with this location, referred to as the galactocentric frame. This frame is not inertial, since the MW and the LMC are orbiting their common COM, but instead is related to the system frame by

$$\mathbf{x} = \mathbf{x}' - \mathbf{x}'_{\text{MW}}(t) \quad (1)$$

$$\mathbf{v} = \mathbf{v}'_{\text{MW}}(t), \quad (2)$$

where the unprimed quantities are in the galactocentric frame and  $\mathbf{x}'_{\text{MW}}$  and  $\mathbf{v}'_{\text{MW}}$  denote the position and velocity of the MW’s center in the system frame, respectively, both of which are functions of time (as explicitly highlighted in this equation). Since  $d\mathbf{v}'_{\text{MW}}/dt \neq 0$ , the galactocentric frame is *not* inertial. The displacement of the galactocentric frame in position and velocity is defined so that at the time of pericenter  $t_{\text{peri}}$  (the present configuration in the actual MW–LMC system)

$$\mathbf{x}(t_{\text{peri}}) = \mathbf{x}' - \mathbf{x}'_{\text{ref}} \quad (3)$$

$$\mathbf{v}(t_{\text{peri}}) = \mathbf{v}' - \mathbf{v}'_{\text{ref}}, \quad (4)$$

where  $\mathbf{x}'_{\text{ref}}$  is the distance between the MW center and the system COM and  $\mathbf{v}'_{\text{ref}}$  is the relative motion of the MW’s center induced by the LMC, also known as the “reflex motion,” which for the real MW–LMC system is approximately  $30\text{--}40 \text{ km s}^{-1}$  at the location of the Sun (D. Erkal et al. 2019; M. S. Petersen & J. Peñarrubia 2020; E. Vasiliev et al. 2021; E. Vasiliev 2023).

The LMC also accelerates the subhalos orbiting in the MW globally, leading to a net bulk motion of these subhalos directed toward the MW–LMC center. The acceleration experienced by an individual subhalo varies depending on its location in the galaxy with respect to the LMC. The LMC would roughly equally accelerate both the subhalos around a stream and the stream itself. However, if subhalos are anisotropically or asymmetrically distributed around the stream, small variations in the accelerations experienced by the subhalos due to the LMC will lead to a perturbatively induced nonzero bulk motion of the subhalos around the stream. In contrast, if the subhalos are isotropically distributed, the net bulk motion around a stream will be zero.

Given that the simulations are run in an arbitrary simulation box frame, the traditional approach is to establish a “principal axis” by aligning the galactic disk to the  $X$ - $Y$  plane at the time of the analog’s first pericentric passage. In this frame, the LMC analog in m12b is located at  $\mathbf{x}_{\text{analog}} = (-23.3, -26.6, 13.7)$  kpc at  $T_{\text{peri}}$ . However, we establish an additional “rotated axis,” which aligns the position unit vector of the LMC analog in m12b at its first pericentric passage with the position unit vector of the *real* LMC in the MW at its first pericentric passage, located at  $\mathbf{x}_{\text{LMC}} = (2.3, -20.2, -41.1)$  kpc, based on the orbits presented in N. Garavito-Camargo et al. (2019). Details on how to compute this rotation can be found in Appendix A.

Figure 1 plots the trajectory of the LMC analog (red/green) in m12b in the rotated axis galactocentric coordinates, along with the total distance from the MW’s central location (on the bottom right), compared to an MW–LMC constrained simulation (blue) from N. Garavito-Camargo et al. (2019). The green sections of the trajectories indicate the periods over which we compute encounter rates. The overall orbit and the present-day location of the analog match reasonably well those of the LMC. Unless otherwise noted, all analyses and results in this paper are presented in the rotated axis frame.

We will compute the subhalo–stream encounter rates for streams distributed in four quadrants in the sky. We define each quadrant in the galactocentric-rotated axis frame in Table 2 for reference, also marked in the Figure 1  $Y$ - $Z$  panel.

Finally, to compute quantities relevant to stream–subhalo encounters, the relevant frame is the one moving with the stream, here referred to as the stream-centric frame. Since most of the currently known streams are closer to the MW center than the LMC, we will relate the stream-centric frame, denoted by  $\tilde{\mathbf{x}}$  and  $\tilde{\mathbf{v}}$ , to the galactocentric frame  $\mathbf{x}$ ,  $\mathbf{v}$  (for streams orbiting beyond the LMC one would substitute the system frame  $\mathbf{x}'$ ):

$$\tilde{\mathbf{x}} = \mathbf{x} - \mathbf{x}_{\text{str}}(t) \quad (5)$$

$$\tilde{\mathbf{v}} = \mathbf{v} - \mathbf{v}_{\text{str}}(t), \quad (6)$$

**Table 2**  
Quadrant Cutoffs in Sky Coordinates

Quadrant	No.	$\phi$ (deg)	$\theta$ (deg)
Northeast	I	−180 to 0	0–90
Northwest	II	0–180	0–90
Southwest	III	0–180	−90 to 0
Southeast	IV	−180 to 0	−90 to 0

**Note.** Here  $\phi$  and  $\theta$  correspond to azimuth and altitude, respectively, in Mollweide projection. Refer to Figure 5(b) for a visual representation.

where  $\mathbf{x}_{\text{str}}(t)$ ,  $\mathbf{v}_{\text{str}}(t)$  are the position and velocity, respectively, of a representative particle in the stream in the galactocentric coordinates (in other words, the stream’s representative orbit). The relevant quantity for determining the rate of subhalo interactions is the distribution of the subhalos velocities perpendicular to the stream, which corresponds to the cylindrical radial velocities of subhalos in this stream-centric frame  $\bar{v}_R$ .

### 2.3. Integrating Stellar Stream Orbits

In order to compute the encounter rates, we need to inject stellar streams into the simulations and integrate their orbits; here we describe the methodology we employ.

#### 2.3.1. Stellar Stream Injection Scheme

Each stream is represented as a test particle that is integrated using the time-dependent potential of the system. We generate two sets of stream catalogs: one resembling the MW streams, and one a synthetic catalog of 5000 streams. The properties and the initial conditions (ICs) used to generate these two catalogs are described below:

1. MW streams: 97 streams orbiting the MW with phase-space properties resembling the observed streams of the MW. We use `galstreams` (C. Mateu 2023) to compute the median phase-space values of each stream. We then inject the stream’s positions and velocity into our rotated axis frame, aligning the orientation of the streams and the LMC analog in our model with that of the real LMC.
2. Synthetic streams: We generate 5000 synthetic stream test particles uniformly spread across the sky in a Mollweide projection and different orbital properties. We simulate these streams to be at their pericenter, with distances between 20 and 80 kpc from the galactic center at  $T=0$  Gyr and varying azimuthal velocities and inclination velocities such that the total tangential velocities at  $T=0$  Gyr are between 250 and 400  $\text{km s}^{-1}$  (set by the real MW streams). These initial conditions produce a uniform distribution of streams’ orbital eccentricities and pericentric distance in all quadrants.

These ICs are used to start the orbital integration for each stream at  $T=0$  Gyr. We then integrate the orbits for a total of 0.5 Gyr, corresponding to the shaded green band in Figure 1 around the pericenter of the LMC-like satellite. We integrate backward for  $-0.4$  Gyr starting at  $T=0$  Gyr and then forward by 0.1 Gyr starting from  $T=0$  Gyr. A value of 0.5 Gyr is sufficient to induce noticeable morphological changes in a stream’s structure, such as the emergence of open gaps and the

occurrence of kinks (D. Erkal & V. Belokurov 2015a). In the following section, we describe the time-dependent model that we use in our orbital integration.

#### 2.3.2. Orbit Integration of Streams

To integrate the orbits of the test particles (each representing a stream), we use time-evolving potential models from A. Arora et al. (2022) following the scheme described in A. Arora et al. (2024). In short, we fitted the potentials with basis function expansions (BFEs) on the host halo at every snapshot in the simulations within the 20 snapshots that span the 0.5 Gyr around the  $T=0$ . These models can adequately describe deformations in the halo caused by the LMC analogs (e.g., M. S. Petersen & J. Peñarrubia 2020; N. Garavito-Camargo et al. 2021; A. Arora et al. 2022; M. S. Petersen et al. 2022). BFEs have also been shown to successfully reproduce orbits, even in the presence of massive satellites, for short periods of time (less than 1 Gyr) in both idealized simulations (E. Vasiliev 2024; S. Lilleengen et al. 2023) and cosmological simulations (B. Lowing et al. 2011; J. L. Sanders et al. 2020; A. Arora et al. 2024).

Since we represent each stream by the orbit of a single test particle, we do not simulate the perturbations along the leading and trailing arms of the stream (as is observed, e.g., in the real-life Orphan stream; S. Lilleengen et al. 2023).

The integration is performed in the principal axis frame on which the BFE models are fit. Nonetheless, we report our results in the rotated axis frame. Our orbit integration of subhalos and streams is not entirely self-consistent, as the subhalos respond to the LMC analog in a live simulation, while the streams are integrated within a smooth, time-evolving potential model. However, one can simply integrate the subhalo orbits within the time-dependent potential using a prescription to account for tidally destroyed subhalos and count flybys. This approach is certainly feasible, but it also relies on the assumption that subhalo orbits can be properly reproduced, without taking into account the effects of dynamical friction.

We use the integrated orbits to calculate the apocenter and pericenter distances, and we categorize the streams as prograde or retrograde relative to the orbit of the LMC analog in m12b. Only about 13 of the known MW streams have pericenter distances greater than 20 kpc from the galactic center in the m12b potential.

### 2.4. Subhalo Selection

We use the ROCKSTAR halo finder (P. S. Behroozi et al. 2012a) to identify DM subhalos. Merger trees were constructed to link the catalogs at each snapshot using the `consistent-trees` code (P. S. Behroozi et al. 2012b), as detailed in J. Samuel et al. (2021) and N. Panithanpaisal et al. (2021). Using these halo catalogs, we identify subhalos that are within the MW and brought in by the LMC analog. We impose a mass range of  $10^6 M_{\odot} \leq M_{\text{sub}} \leq 10^9 M_{\odot}$  on all the subhalos based on our resolution. We select the subhalos bound to and within the virial radius of the LMC analog 2 Gyr before the first pericenter, when the  $d_{\text{LMC}} + R_{\text{vir,LMC}}$  is greater than the  $R_{\text{vir,MW}}$ , and track their evolution through time until disruption using `consistent-trees`.

The LMC analog brings a total of 1029 subhalos. Figure 2 plots the location of the LMC-analog subhalos as density contours in the  $X$ - $Z$  plane for m12b at  $-1$  Gyr (left), 0 Gyr (middle), and 1 Gyr (right) with the LMC-analog trajectory and

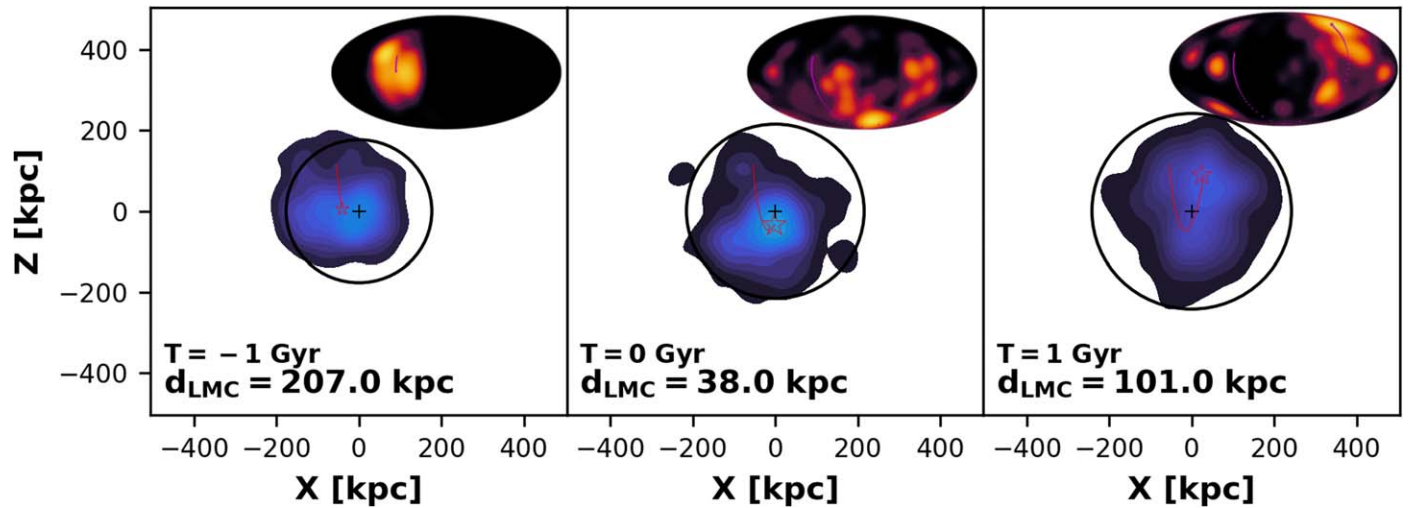


**Figure 2.** Density contours of the surviving subhalos brought in by the LMC analog at three time steps,  $-1$  Gyr (left),  $0$  Gyr (middle), and  $1$  Gyr (right), along with the analog’s trajectory (red) in the  $X$ - $Z$  plane for m12b. The black circle marks the virial radius of the MW, and the upper right inset shows the LMC analog’s subhalo density in Mollweide projection at each time step. As the analog falls in the MW, the LMC-analog subhalos are tidally stripped away from it and settle into bound orbits around the MW. This is obvious at  $0$  and  $1$  Gyr, as the density contours are more widespread in both cases. At  $0$  Gyr, the majority of the subhalos lag behind the infalling LMC analog, while some completely settled into newer orbits, producing a dipole term in density. At  $1$  Gyr, almost all of the subhalos are dispersed away from the LMC analog, as the central density of subhalos is away from the LMC analog. Also note that there is a slingshot action as a few subhalos end up unbound and outside the virial radius of the MW after the analog’s flyby (upper right corner for  $T = 1$  Gyr).

location (shown in red). Insets in the upper right corner show the density of these subhalos in Mollweide projection. The LMC analog starts in the south and falls toward the galactic center, bringing its own population of subhalos that are widely distributed in different regions and settle into newer bound orbits around the MW as the merger proceeds. Note the trailing subhalos behind the satellite at pericenter in both the Cartesian plane and Mollweide projection. Similar LMC subhalo distributions with leading and trailing arms are noted in L. V. Sales et al. (2017).

We track whether these subhalos are bound to the LMC analog or the MW using a total negative energy criterion (i.e.,  $E_{\text{sub,tot}} \leq 0$  in the LMC analog or the MW reference frame). We also note whether the subhalos merge into the LMC analog or the MW. A subhalo is considered “merged” when `consistent-trees` can no longer track its center and its descendant subhalo links to either the MW or the LMC analog. `consistent-trees` can successfully track subhalos with masses greater than  $10^6 M_{\odot}$  (J. Samuel et al. 2021).

Figure 3 illustrates the number of LMC-analog subhalos bound to the LMC analog (blue) or the MW (orange), merged into the LMC analog (green) or the MW (red) as a function of time starting from 2 Gyr before the first pericenter passage. By the first pericenter ( $0$  Gyr), 80% of the subhalos are tidally stripped from the satellite and bound to the MW. By 1 Gyr, only half of the subhalos survive the merger, while the rest are destroyed and form dark streams. In the scope of our simulations, and given our inability to resolve these dark streams, we leave them out of our calculations for future research. These dark streams are less likely to leave observable signatures after their interactions with stellar streams because of their low surface density.

### 2.5. Stream–Subhalo Encounter Rates

Counting the number of stream–subhalo encounters is not feasible, due to the limited temporal resolution in the simulations. Our time range consists of approximately 20

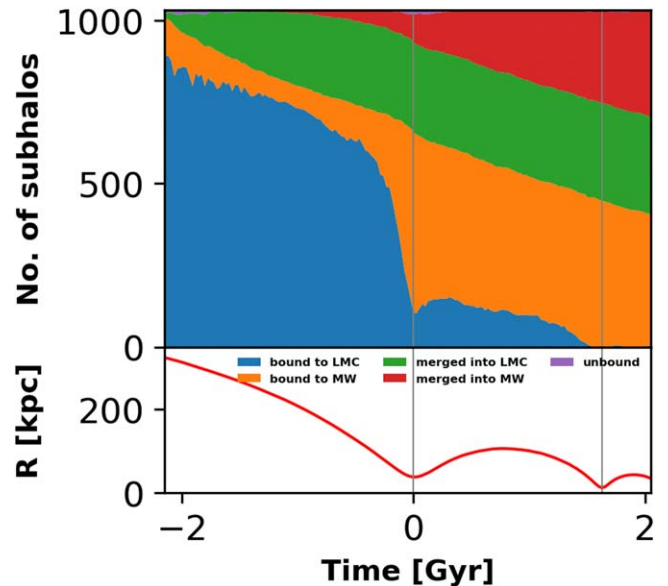


**Figure 3.** The bound properties of 1029 LMC-analog subhalos with mass range  $10^6 M_{\odot} \leq M_{\text{sub}} \leq 10^9 M_{\odot}$  at different time steps to illustrate whether they are still bound to the LMC analog (blue), bound to the MW (orange), or merged into the MW (red) or the LMC analog (green). The number of subhalos bound to the analog drastically drops after the first pericentric passage, where the tidal forces from the MW are stronger and hence they become bound to the MW. By the second pericenter passage, most of the subhalos either are bound to the MW or have been completely tidally stripped. Only about 50% of subhalos survive after the merger is complete. The number of subhalos brought in by the LMC analog that merged into it (green) increases as the analog gets closer to the MW but remains constant after the first pericenter, while more subhalos merge into the MW (red) as the merger proceeds. Note that the few unbound subhalos at  $0$  Gyr are due to the instability of the potential model to accurately describe the MW–LMC system.

snapshots, each spaced 25 Myr apart. Therefore, we calculate the encounter rate at each snapshot from our simulation between the subhalos and a stellar stream using the counting scheme described by D. Erkal et al. (2016), which is similar to

the one conducted by J. H. Yoon et al. (2011). The encounter rates are computed as the number of subhalos entering a cylinder of radius  $b_{\max}$  (impact parameter) around a straight line stream of length  $\ell_s$ . The encounter rates depend on the local number density of subhalos  $n_{\text{sub}}$  around the stream and the cylindrical radial velocity  $\tilde{v}_R$  distribution of subhalos with respect to the stream.

The number of subhalos passing through a cylinder of length  $\ell_s$  and radius  $b_{\max}$  at time  $t_{\text{snap}}$ , within a time interval  $dt$ , is then given by

$$dN_{\text{enc}}(t_{\text{snap}}) = (2\pi b_{\max} \ell_s) \cdot (|\tilde{v}_R| dt) \cdot n_{\text{sub}} \cdot P(\tilde{v}_R) d\tilde{v}_R. \quad (7)$$

Here  $P(\tilde{v}_R)$  represents the probability distribution function of  $\tilde{v}_R$ . In contrast to D. Erkal et al. (2016), where they considered a straight line stream of length  $\ell_s$  and computed encounter rates by modeling a cylinder of length  $\ell_s$  and radius  $b_{\max}$  around the stream, our approach simplifies the stream to a single-particle representation. This approximation does not accurately describe a cylinder around the stream. Instead, we calculate  $\tilde{v}_R$  as the relative velocity component perpendicular to the tangent plane of the stream at  $\hat{x}_{\text{str}}$  as  $\tilde{v}_R = (\mathbf{v}_{\text{sub}} - \mathbf{v}_{\text{str}}) \cdot \hat{x}_{\text{str}}$ , with direction toward the plane, from both the top and bottom of the plane, represented with negative values. This approach overlooks the orientation of the stream on the tangent plane itself. Subhalos moving toward the plane with a zero component perpendicular to the plane can still perturb the stream, an effect not accounted for in our single-particle model. Therefore, we integrate over different orientations of the plane assuming that  $P(\tilde{v}_R)$  remains symmetric under small rotations, imitating the change in direction of the normal to the cylinder. This produces an extra factor of  $2\pi$ . In this calculation, we consider only subhalos entering through the sides of the ‘‘cylinder,’’ so we integrate over all negative  $\tilde{v}_R$ . We can then rewrite the encounter rates as

$$\frac{dN_{\text{enc}}}{dt}(t_{\text{snap}}) = (2\pi b_{\max} \ell_s) \cdot n_{\text{sub}} \cdot \mathcal{I}(\tilde{v}_R) \quad (8)$$

$$\mathcal{I}(\tilde{v}_R) \equiv \int_{-\infty}^0 |\tilde{v}_R| \cdot P(\tilde{v}_R) d\tilde{v}_R, \quad (9)$$

where  $\mathcal{I}(\tilde{v}_R)$  is the first moment of the probability distribution of subhalos entering the cylinder ( $\tilde{v}_R \leq 0$ ).  $P(\tilde{v}_R)$  is often approximated by a Gaussian distribution of  $\tilde{v}_R$  assuming a nonzero mean ( $\tilde{\mu}$ ) and dispersion ( $\tilde{\sigma}$ ) (J. H. Yoon et al. 2011; D. Erkal et al. 2016). In such a scenario,  $\mathcal{I}(\tilde{v}_R)$  simplifies to

$$\mathcal{I}_{\text{gauss}}(\tilde{v}_R) = \frac{\tilde{\sigma}}{\sqrt{2\pi}} \cdot f(\tilde{\gamma}),$$

$$\text{where } f(\tilde{\gamma}) \equiv e^{-\tilde{\gamma}^2} + \sqrt{\pi} \tilde{\gamma} (\text{erf}(\tilde{\gamma}) - 1), \quad (10)$$

where  $\tilde{\gamma} \equiv \frac{\tilde{\mu}}{\sqrt{2}\tilde{\sigma}}$ . Parameter  $f(\tilde{\gamma})$  is a unitless scaling factor that depends on the mean and dispersion of  $\tilde{v}_R$ , hereafter the anisotropic boost factor. This factor equals unity when  $\tilde{\mu} = 0$  (see Figure 15 in Appendix B for more details) for the traditional encounter rate formulation such as in J. H. Yoon et al. (2011), D. Erkal et al. (2016), and M. Barry et al. (2023). In Appendix B, we demonstrate that this approximation is valid to within 10% error compared to the numerical integration.

The density of subhalos,  $n_{\text{sub}}$ , is computed as a function of time by counting the number of subhalos within a 10 kpc width

spherical shell centered around the stream. This shell is further confined to a sky slice that spans  $\pm\pi/2$  in colongitude and  $\pm\pi/4$  in colatitude around the stream’s position. The stream is always positioned at the center of this slice at each time step. We then divide the counts by the volume of this sliced shell, which is one-fourth of the total volume of the spherical shell. Our decision not to use a local volume around the stream was made to mitigate numerical noise owing to low subhalo counts. Similarly, we evaluate  $P(\tilde{v}_R)$  from subhalos within the same shell and in the stream’s quadrant for each time step of the stream. We numerically integrate Equation (9) using  $P(\tilde{v}_R)$  to compute the encounter rates for each time snapshot using Equation (8).

Finally, we sum the number of encounters per gigayear for a stream using the equation

$$\frac{N_{\text{enc}}}{\text{Gyr}} = \frac{\sum_{t_{\text{snap}}} \frac{dN_{\text{enc}}}{dt}(t_{\text{snap}}) \Delta t_{\text{snap}}}{\sum_{t_{\text{snap}}} \Delta t_{\text{snap}}}, \quad (11)$$

where  $\Delta t_{\text{snap}}$  represents the time interval between snapshots, the sums are taken over all time steps  $t_{\text{snap}}$ , and  $\frac{dN_{\text{enc}}}{dt}$  is computed using Equation (8).

In this paper we do not explore the impacts caused by any single encounters in our analysis, which are more sensitive to the individual stream and subhalo kinematics and require a case-by-case study. We rather focus on a global analysis of the encounter rates in this paper. Traditionally an impact weighting based on the impulse approximation  $\sim \frac{GM_{\text{sub}}}{v^2 b}$ , where  $b$  is the distance of the closest approach between a subhalo and a stream, has been used in the literature (D. Erkal & V. Belokurov 2015a; D. Erkal et al. 2016). However, implementing such weighting in our method would require integrating over the mass distribution of subhalos, which is trivial since  $P(M_{\text{sub}}) \propto 1/M_{\text{sub}}$ , and a distribution of  $b$ . Finding  $b$  requires computing pairwise distance between each stream and all the subhalos within some set distance cutoff around the stream during the integration time, and the number of subhalos changes nontrivially. Alternatively, one can assume that  $b$  is a nonlinear function of the velocity perpendicular ( $\tilde{v}_R$ ) and parallel ( $\tilde{v}_{\parallel}$ ) to the stream. These assumptions lead to a coupled 2D integral with both the velocity distributions in the denominator and  $\sqrt{\tilde{v}_R^2 + \tilde{v}_{\parallel}^2}$  in the numerator; this integral diverges at 0 and is highly sensitive to minor fluctuations. However, in our case the impact weighting for the subhalos brought in by the LMC analog will be similar to the impact weighting of the MW subhalos; this is demonstrated by showing that the velocity field is fairly independent of the subhalo mass in Section 3.

### 3. Effects of Massive Satellites on Encounter Rates

In this section, we illustrate how and why each of the physical quantities in the encounter rates (subhalo number density and radial velocity distribution) is affected during the infall of the LMC analog. In Section 3.1 we start by exploring the temporal evolution of the phase-space distribution of the host and contributed subhalos. In Section 3.2 we explore the temporal changes in the radial velocity distribution of the subhalos caused by the perturbations of the LMC analog. In Section 3.3 we explore the radial and angular variations on the sky in the integral of the probability distribution  $\mathcal{I}(v_{\text{rad}})$ . Lastly, we quantify the evolution of the number density of subhalos in Section 3.4.

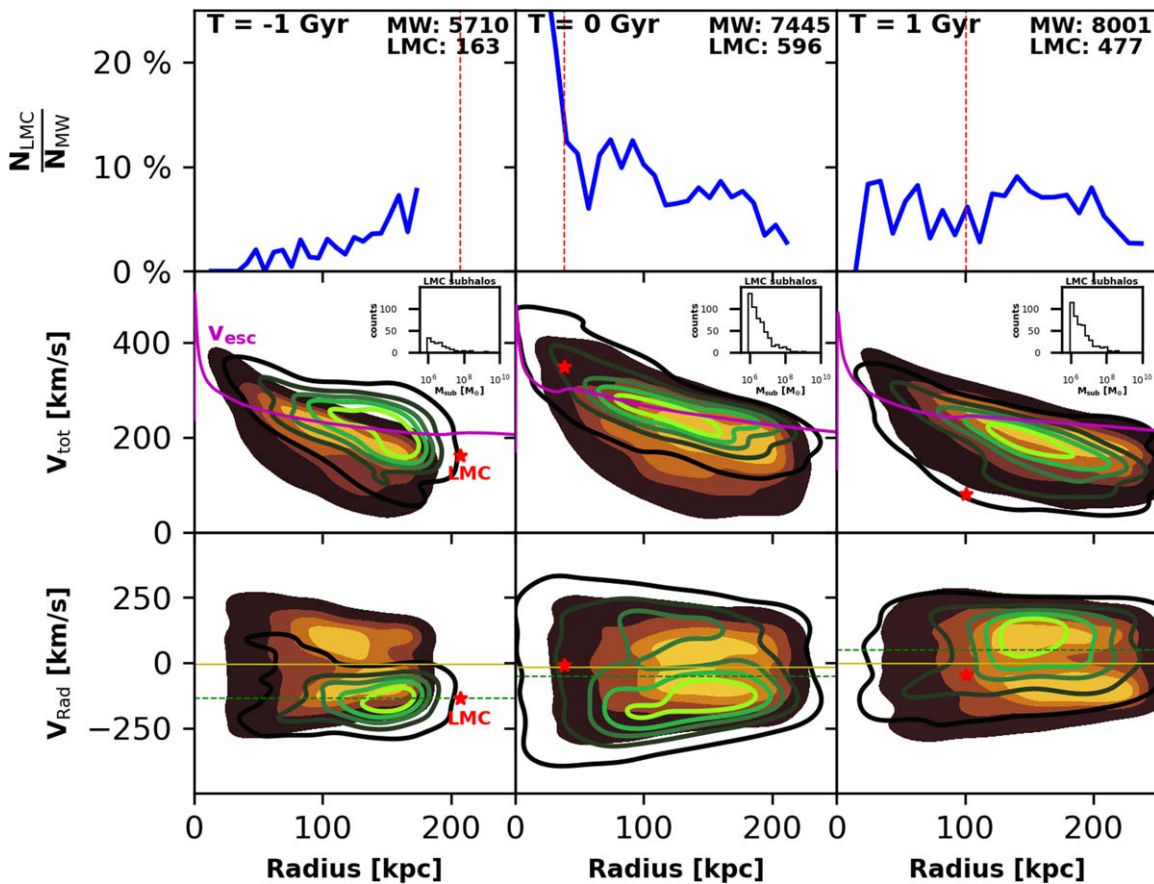


**Figure 4.** Phase-space evolution of the MW subhalos and the LMC analog contributed subhalos within the MW’s virial radius. Each column shows the distributions at different times:  $-1$  Gyr (left),  $0$  Gyr (middle), and  $1$  Gyr (right). Top row: fraction of the contributed subhalos as a function of distance. Only a small fraction of subhalos (less than 10%) are brought in by the LMC analog, yet they induce significant changes (around 20%) in the spherically averaged subhalo number density near  $T = 0$  Gyr, especially around the LMC analog’s pericentric distance. The red dashed line shows the location of the LMC analog in each snapshot. Middle: the total velocity distribution in the galactocentric coordinates vs. radius for the MW background (filled contours) and the contributed (open contours) subhalos, along with the host’s escape velocity curve (magenta) at each time. Insets show mass distribution of the contributed subhalos. The tangential velocity distribution of the subhalos in the galactocentric coordinates shows similar trends to the total velocity distribution. Bottom: the radial velocity in the galactocentric coordinates of the MW subhalos and contributed subhalos is marked by solid yellow and dashed green lines, respectively. The red star marks the LMC analog’s location. Both of the phase spaces stabilize after the first pericenter. By  $T = 1$  Gyr, the contributed subhalo distribution matches the MW background as the subhalos undergo phase mixing.

### 3.1. Phase-space Distribution of the Perturbed Subhalo Population

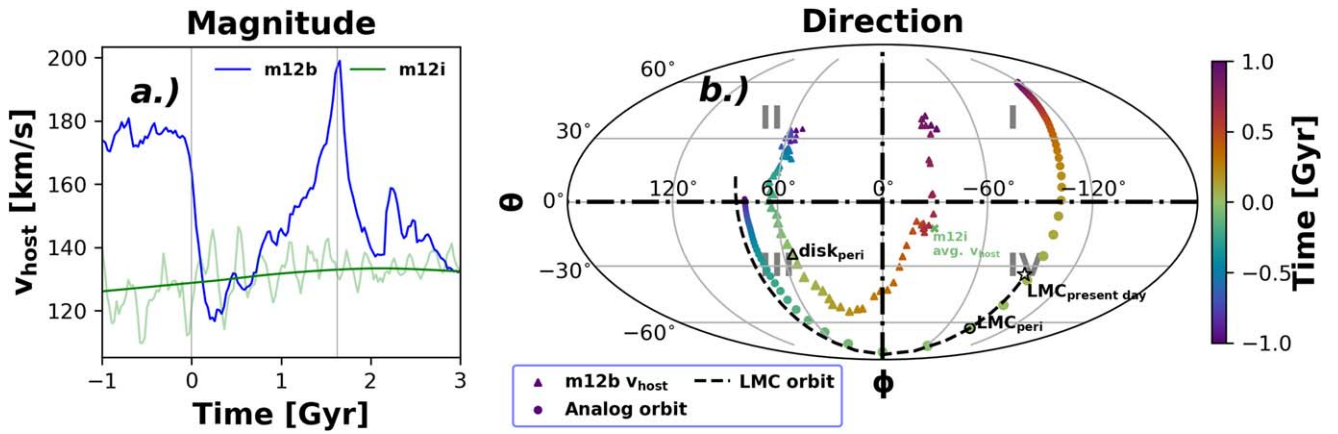
We begin by characterizing the phase-space distribution of both the host subhalos (those within the virial radius of the MW and not brought in by the LMC analog) and the subhalos brought in by the LMC analog, hereafter the *contributed* subhalos. We show how the presence of these subhalos influences the overall phase-space distribution and dynamics of the MW subhalos.

Figure 4 shows the phase-space distribution at three equally spaced time steps:  $1$  Gyr before pericenter (left column), when the LMC analog is at pericenter (middle column), and  $1$  Gyr after pericenter (right column). The ratio of contributed subhalos to the total subhalos as a function of radius is plotted in the top row. Despite the contributed subhalos composing only a fraction (less than 10%) of the host subhalos, they can increase the spherically averaged subhalo density near the LMC analog’s radial distance (indicated by the red dashed line) by up to 20%.

The middle and bottom rows show the total velocity and radial velocity distributions in the galactocentric coordinates of the contributed subhalos (depicted as open contours), relative to the background MW subhalo distribution (depicted as filled

contours) within the virial radius of the MW. Notably, both the distributions of the contributed subhalos within the virial radius reveal a distinct leading arm (higher density closer to the host center) compared to the LMC analog (indicated by the red star) and exhibit different phase-space characteristics compared to the MW. As the merger progresses, the surviving subhalos gradually phase-mix into new orbits resembling those of the MW subhalos, which becomes evident as early as  $1$  Gyr after the first pericentric passage, aligning with findings in L. V. Sales et al. (2017) and M. Barry et al. (2023). The tangential velocity distribution of the subhalos (not shown in the figure) in the galactocentric coordinates mirrors the trends seen in the total velocity distribution. The escape velocity curves are overlaid in the middle row at each time step. Most of the subhalos are below the escape velocity; however, some exhibit higher total velocities. Many of these subhalos are falling toward the galactic center and thus experience tidal stripping. The insets in the upper right corner of the middle row show the mass distribution of the contributed subhalos within the virial radius.

It is important to highlight that the LMC analog’s position is not centered within the open contour distribution. This is



**Figure 5.** (a) COM velocity of the m12b (blue) and m12i (green) hosts as a function of time. The rapid change of  $60 \text{ km s}^{-1}$  in the host velocity of m12b is evident as the LMC analog passes its first pericenter position at  $T = 0 \text{ Gyr}$  (indicated by the gray line), leading to another spike at  $T = 1.6 \text{ Gyr}$  (the second pericenter passage). Eventually, the effect stabilizes as the LMC analog undergoes tidal stripping around the MW’s potential. No such changes are noted in m12i. (b) The triangles mark the unit vector of the relative central velocity in spherical coordinates quantifying the directional response of the MW center to the LMC-analog orbit marked with circles for m12b as a function of time (color bar). The size of the markers is relative to the proximity of the LMC analog to the MW center. The MW center moves toward the direction of the LMC analog, with the maximum degree of dislodgement occurring at  $T = 0 \text{ Gyr}$ . We only show the average direction of the MW center response (marked with a green cross) for m12i, as no distinct trends are observed. The dashed line shows the orbit of the LMC from N. Garavito-Camargo et al. (2019) up to the present day.

because we are solely analyzing the subhalos situated within the MW’s virial radius.

Furthermore, at  $T = -1 \text{ Gyr}$ , the mean radial velocity of the contributed subhalos is  $\approx 150 \text{ km s}^{-1}$  (marked by the green dashed line), corresponding to the analog’s radial velocity. By  $T = 0 \text{ Gyr}$ , the mean radial velocity of the surviving contributed subhalos aligns within  $\pm 25 \text{ km s}^{-1}$  of the MW subhalo population as they experience phase mixing.

In summary, the presence of contributed subhalos can increase the spherically averaged subhalo density by up to 10%–40% (Appendix C); M. Barry et al. (2023) note a higher boost due to the contributed subhalos in other LMC analogs. This effect will become more pronounced when considering the azimuthal dependence of the subhalo density distribution. Surviving LMC-analog subhalos gradually phase-mix into orbits resembling the MW subhalos. However, before  $T = 0 \text{ Gyr}$ , the contributed subhalos can shift the mean radial velocity of subhalos, thus affecting the stream–subhalo encounter rates (Equation (8)). These effects are most prominent during the first pericentric passage and can either increase or decrease the encounter rates.

### 3.2. Temporal and Radial Evolution of the Subhalo Velocity Distribution

The local subhalo density and velocity distributions are not only affected by the contribution of additional subhalos from the LMC analog; they are also perturbed by the shift of the COM frame induced by the presence of the LMC analog. To illustrate this, we show in Figure 5(a) the COM velocity of the MW’s host over time for both m12b (blue) and m12i (green) in the reference frame of the cosmological volume. The MW COM is determined using the shrinking spheres method described in C. Power et al. (2003). The total central velocity is calculated using the mean velocities of stars within 10 kpc of the MW’s COM.

As the LMC analog approaches its first pericentric passage, there is a  $60 \text{ km s}^{-1}$  change in the MW central velocity primarily caused by the LMC analog moving the COM of the system away from the host’s center. This persists for 1–1.5 Gyr

after the first pericenter as the LMC analog and the MW orbit their common COM. The effect reaches another peak as the system approaches its second pericenter passage at approximately 1.7 Gyr. In contrast, such motion is not observed in m12i, which has a relatively constant velocity of about  $130 \text{ km s}^{-1}$  in time with deviations of order  $10 \text{ km s}^{-1}$ , consistent with the results from J.-B. Salomon et al. (2023).

In Figure 5(b), we present the direction of unit vectors  $v_{\text{host}}$  of the host with respect to its present-day velocity in spherical coordinates (indicated by triangle markers). We also show the trajectory of the LMC analog (represented by a solid circle marker) as a function of time (color bar) for m12b. Each point on the plot indicates the direction and magnitude of the net velocity of the host. The size of the markers is inversely proportional to the galactocentric distance of the LMC analog. The LMC orbit from N. Garavito-Camargo et al. (2019) is shown with the black dashed line up to the present-day location.

As the LMC analog transitions from the Q.III to the Q.IV and moves closer to the galactic center, the MW COM moves toward the trajectory of the LMC analog. This effect is most pronounced when the LMC analog approaches its first pericenter at  $T = 0 \text{ Gyr}$ . By the time of the LMC analog’s second pericenter, the induced reflex motion is not as strong, as the halo starts to relax and the satellite loses energy. In contrast, m12i does not show a systematic trend with the merging satellite and exhibits a random distribution of velocity vectors. The green cross represents the average central displacement over the duration of the satellite merger.

We now explore how the velocity of the COM of the host changes the radial velocity of the subhalos as a function of time. In Figure 6, we plot the mean radial velocity of subhalos in galactocentric coordinates  $\langle v_{\text{rad}} \rangle$  in multiple 20 kpc radial bins. We observe variations in the mean radial velocities at the LMC analog’s first pericenter ( $T = 0$ ) and in subsequent apocenters and pericenter in m12b for all the subhalos within the virial radius (solid black). These variations are due to both the motion of the COM of the host and the contribution from the LMC-analog subhalo population with its own distinct phase-space properties. Similarly, the mean tangential velocity

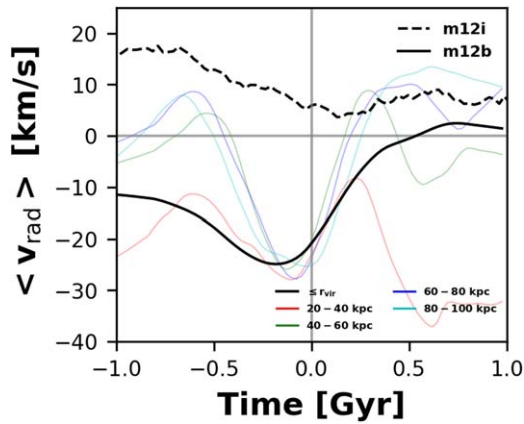


**Figure 6.** The mean radial velocity of all the subhalos in the galactocentric coordinates for m12b (solid lines) and m12i (black dashed line) as a function of time, in different radial bins color-coded. The data are smoothed using the lowest smoothing method (W. S. Cleveland & S. J. Devlin 1988). The mean radial velocity undergoes significant changes in m12b as the LMC analog approaches its first pericentric passage. However, the radial velocity stabilizes again as the LMC analog undergoes tidal stripping. In contrast, m12i exhibits a relatively constant mean radial velocity throughout the time frame (computed within  $r_{\text{vir}}$ ).

of subhalos in the galactocentric coordinates also changes by about  $30 \text{ km s}^{-1}$ . The most significant deviations are observed in the 40–60 kpc bin (solid green) and the 60–80 kpc bin (solid blue), corresponding to the distances probed by the LMC analog during the given time interval. The high variations in the 20–40 kpc bin are attributed to a small number of statistics. m12i (dashed line) demonstrates a relatively low and constant mean value. Interestingly, the velocity dispersion (not shown here) remains relatively constant azimuthally at a radius and in time in both m12i and m12b.

The changes in the velocity distribution of the subhalos also affect the first moment of the velocity distribution  $\mathcal{I}(v_{\text{rad}})$  in the galactocentric coordinates. Here we quantify those changes as a function of time. Figure 7 shows the temporal evolution of  $\mathcal{I}(v_{\text{rad}})$  computed numerically using Equation (9) for subhalos in different mass bins (color-coded). These subhalos orbit within a distance range of 40–80 kpc from the galactic center. The  $\mathcal{I}(v_{\text{rad}})$  for subhalos in different mass ranges exhibits similar trends over time (varying between 50 and  $100 \text{ km s}^{-1}$ ), yet the amplitudes are different by 25%. Notably, there is an increase in  $\mathcal{I}(v_{\text{rad}})$  right before the LMC analog’s first pericentric passage at 0 Gyr as a result of the COM motion of the host. The black curve, which accounts for all subhalos, closely matches the lower mass bin curves, reinforcing that the overall trend is consistent. The high jitter observed in the  $10^{7.5}–10^9 M_{\odot}$  mass range results from small number statistics, which causes fluctuations in the integral and affects its convergence owing to the lower number of subhalos in this mass bin. The consistency in  $\mathcal{I}(v_{\text{rad}})$  highlights that the overall velocity field is mostly decoupled to the mass and density field of subhalos. While we have only considered spherically averaged effects here, this decoupling between the velocity field and the mass of the subhalos is expected to persist even in spatially localized regions.

### 3.3. Distance and Azimuthal Dependence of $\mu$ and $\sigma$

As we have demonstrated in Section 3.1, the location of the contributed subhalos from the LMC analog varies as the

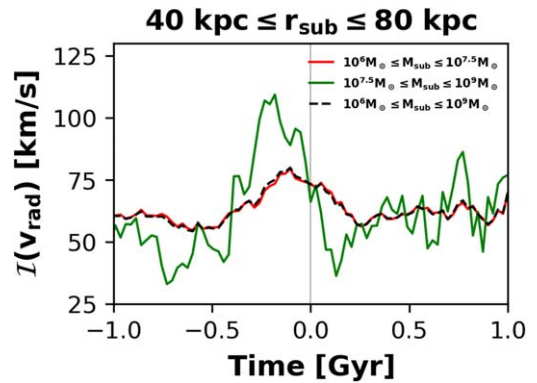


**Figure 7.** The probability distribution integral from Equation (9) as a function of time computed using the 3D radial velocity distribution ( $v_{\text{rad}}$ ) in galactocentric coordinates of subhalos in low ( $10^6–10^{7.5} M_{\odot}$ ; red) and high ( $10^{7.5}–10^9 M_{\odot}$ ; green) mass bins, and all the subhalos (black) orbiting at a distance of 40–80 kpc from the galactic center.  $\mathcal{I}(v_{\text{rad}})$  for different mass bins show similar variation and behavior. An overall increase in  $\mathcal{I}(v_{\text{rad}})$  is noted right before the first pericentric passage at 0 Gyr. The high jitter observed for the  $10^{7.5}–10^9 M_{\odot}$  mass bin arises from small number statistics, which affects the convergence of the integral owing to the low number of subhalos in this high mass bin.

satellite orbits the host. Moreover, due to the host’s COM motion, the radial velocities of the entire population of subhalos change as a function of radius and time. Here we further explore the angular variations that the radial velocity distribution induces in the  $\mathcal{I}(v_{\text{rad}})$ . To simplify our calculation, we assume that the radial velocity distribution around the streams is Gaussian. We found this approximation to be accurate at the 10% level as shown in Appendix B. However, we do not assume that the mean velocity of the radial velocity distribution  $\tilde{\mu}$  is zero. To quantify the degree of asymmetry in different regions of the sky, we compare our results to the case of  $\tilde{\mu} = 0$ .

In Figure 8, the top panel plots the LMC-analog distance from the center as a function of time, with the LMC analog’s quadrant marked with shaded color regions at each time step. We also show selected 20 kpc bins within the 20 and 80 kpc interval, based on the LMC analog’s location. In the middle panel, we plot the change in the anisotropic boost factor, that is,  $[f(\gamma) - f(0)]$ , as a function of time in the selected 20 kpc bins (shown in the top panel) for m12b with contributed subhalos (labeled as m12b; dark blue) and without contributed subhalos (labeled as m12b (without LMC subhalos); magenta) and m12i (green), the galaxy without massive satellites. The bottom panel shows the change in the anisotropic boost factor within the 60–80 kpc bin in the quadrant polar opposite to the LMC analog at each time step. In addition, these calculations act as proxies for streams in a fully circular orbit centered in each bin in the respective quadrants.

The anisotropic boost factor in m12b both with and without contributed subhalos increases up to 60% as the LMC analog approaches its first pericenter. While both cases for m12b show a positive increase (a positive net inflow of subhalos in the bin), m12b with contributed subhalo trends is consistently higher than m12b without contributed subhalos by approximately 20%. The trend increase in m12b without the contributed subhalos is caused by the analog’s effect on the velocity distribution parameters locally. As the contributed subhalos begin to experience tidal stripping, the trends in both cases for m12b converge at around 0.1 Gyr. We note a boost of about 40% right after the first pericentric passage, mostly in Q.

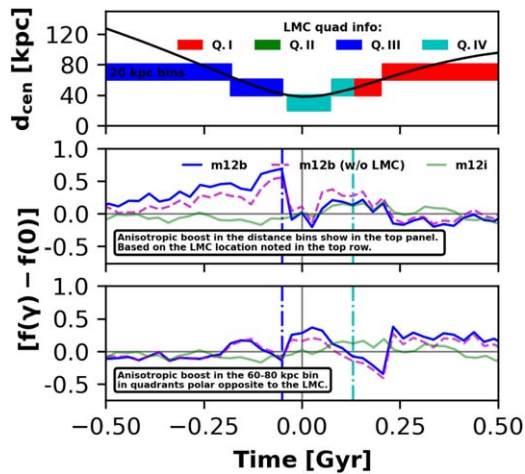


**Figure 8.** The top row plots the distance from the center of the LMC analog as a function of time along with the distance bins of width 20 kpc in different quadrants (color-coded) as shaded regions. The middle row plots the change in anisotropic boost factor  $[f(\gamma) - f(0)]$  (in galactocentric coordinates; refer to Equation (10)) as a function of time for m12b with contributed subhalos (dark blue), m12b without contributed subhalos (magenta), and m12i (green) evaluated in the distance bins and quadrants marked in the top row and in the 60–80 kpc bin in the quadrants polar opposite to the LMC (bottom row). Both cases with and without contributed subhalos exhibit up to a 60% increase in the boost factor around the LMC analog, with peak effect just before  $T = 0$  Gyr. The outermost regions opposite to the LMC analog also experience a higher boost of about 40% after the first passage. m12i, the galaxy with no massive satellites, shows a variation of approximately 10% attributed to halo evolution. These values can be attributed to computations corresponding to a stream assumed to be in a fully circular orbit at the center of each distance bin in the respective quadrant.

II in the outer bin owing to the reflex motion as the LMC analog moves from Q.III to Q.IV. For m12i (green), the variation in boost factor stays within  $\pm 10\%$ , primarily influenced by the halo evolution and the observed anisotropic velocity distribution (E. C. Cunningham et al. 2019).

### 3.4. Impact on the Local Subhalo Density

The LMC analog perturbs the number density  $n_{\text{sub}}$  of subhalos in two distinct ways.

First, it introduces an anisotropically distributed subhalo population that is dragged along by the satellite’s motion. Second, it induces a response in the MW’s DM halo. As the LMC approaches its first pericentric passage, the inner galaxy (consisting of the disk and halo system within 30 kpc) reacts more rapidly than the outer galaxy, resulting in a relative displacement between the two reference frames: the inner and outer galaxy frames. This displacement gives rise to a north–south asymmetry in density, which is referred to as the collective response (N. Garavito-Camargo et al. 2021; J.-B. Salomon et al. 2023). The collective response includes a large-amplitude weakly damped dipole mode, as well as several other low-amplitude modes (M. D. Weinberg 2023). Additionally, the satellite induces a trailing dynamical friction wake in the DM halo (N. Garavito-Camargo et al. 2019).

Figure 9 plots the total number of subhalos within the virial radius of the MW in decades of total subhalo mass for the MW subhalos (black) and MW subhalos combined with LMC-contributed subhalos (green) at equally spaced times:  $-1$  Gyr (left),  $0$  Gyr (middle),  $1$  Gyr (right). The insets in each panel plot the fraction of LMC to MW subhalos as a function of each mass decade, and this fraction is found to remain fairly

consistent (10%–20%) around 0 Gyr. This indicates that the subhalos contributed by the LMC analog do not have significantly different masses compared to the MW subhalos.

Figure 10 illustrates the variation in the number of subhalos over time in each quadrant for the inner halo (0–50 kpc; top row) and the outer halo (50–100 kpc; bottom row) in the case of m12b with and without contributed subhalos (left and middle columns, respectively), as well as for m12i (right column). The color bar at the bottom represents the quadrant location of the LMC analog in m12b during a time interval of  $\pm 0.5$  Gyr.

For m12i, the number of subhalos remains relatively consistent across all quadrants over time, except for Quadrant IV in the outer halo, where the systematically increased subhalo population is caused by the presence of an orbiting dwarf galaxy.

In the case of m12b, we identify the specific effects that contribute to perturbations in the number of subhalos within a time interval of approximately  $\pm 0.5$  Gyr. Q.I has the major contributions from a combination of collective response and leading contributed subhalos.

1. *Contributed subhalos.* We observe a relative increase in the number of subhalos in the outer halo Q.III (between  $-0.3$  and  $-0.05$  Gyr), Q.IV (between  $-0.05$  and  $0.13$  Gyr), and Q.I ( $0.13$  Gyr onward) when comparing the left and middle columns. Additionally, there are enhancements in Q.IV of the inner halo at 0 Gyr, corresponding to the satellite being at a pericenter distance of 38 kpc.
2. *Collective response.* A significant overdensity is observed in the outer halo (middle column), primarily in Q.I and Q.II, as the satellite approaches pericenter in Q.IV (starting from approximately  $-0.5$  Gyr).
3. *DM dynamical friction wake.* The middle column shows a consistent number of subhalos after the LMC analog leaves a specific quadrant. In the outer halo, the subhalos predominantly trail the LMC analog in Q.III (near 0 Gyr) and Q.IV (between  $0.12$  and  $0.25$  Gyr).

These effects collectively contribute to the observed perturbations in the number density of subhalos and their respective quadrants within the specified time interval for m12b.

## 4. Encounter Rates for Simulated and Real Streams

In this section, we present our results for the stream–subhalo encounter rates for the synthetic streams (Section 4.1) and the MW streams (Section 4.2). These encounter rates are calculated using Equation (8) for each time step along the integrated stream orbits computed by directly integrating Equation (9) without applying any Gaussian assumptions. We subsequently compute the average encounter rates per gigayear using Equation (11). We report the number of encounters per gigayear per stream length  $\ell_s$  per maximum impact parameter  $b_{\text{max}}$ , denoted as  $\frac{N_{\text{enc}}}{\text{Gyr}}$  with  $\tilde{\mu} \neq 0$ .<sup>9</sup> We also utilize the more traditional approach involving setting  $\tilde{\mu} = 0$ , denoted as encounter rates with  $\tilde{\mu} = 0$ , for the anisotropic boost factor as described in Equation (10). For m12b, we further compute the encounter rates by excluding the contributed subhalos, denoted as encounter rates without the LMC. Our simulations

<sup>9</sup> The notation  $\tilde{\mu} \neq 0$  is used here, but the rates are computed by directly integrating Equation (9) without applying any Gaussian assumption.

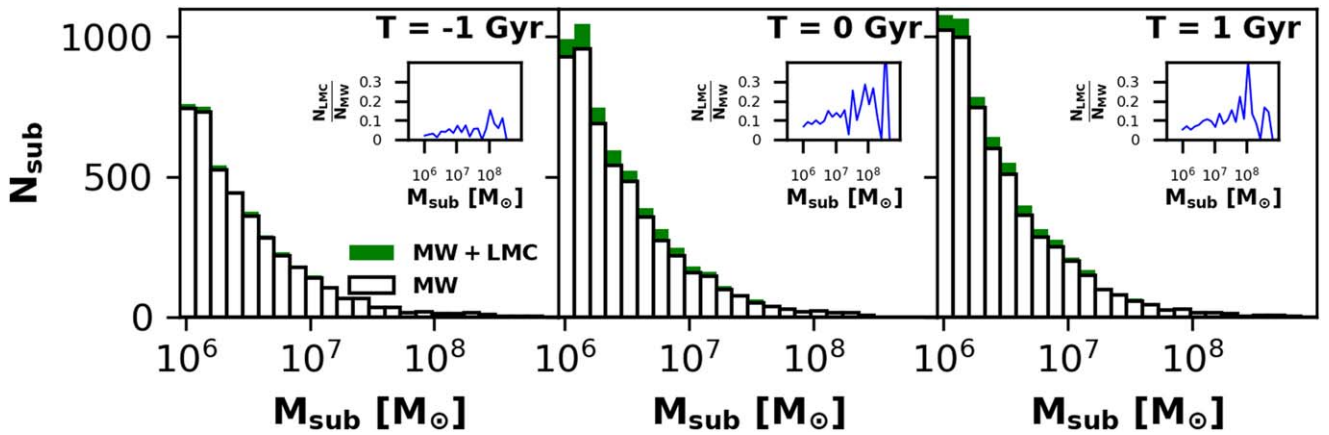


**Figure 9.** The total number of subhalos in each decade of mass for the MW subhalos (black) and MW subhalos combined with those contributed by the LMC analog (green) that are within the virial radius of the MW at different times:  $-1$  Gyr (left),  $0$  Gyr (middle), and  $1$  Gyr (right). The insets in each column plot the fraction of LMC to MW subhalos in different mass bins. Around  $0$  Gyr, the fraction of contributed subhalos are roughly similar (10%–20%) across bins of mass  $\leq 10^8 M_{\odot}$  (dark subhalos). Higher fractions of subhalos with masses  $\geq 10^8 M_{\odot}$  arise from small number statistics. The contributed subhalo fractions are higher in spatially localized regions (see Figure 4 and Figure 10).

are limited by the subhalo resolution and the presence of artificial disruption near the LMC analog (F. C. van den Bosch et al. 2018; S. B. Green et al. 2021), which might lead to a systematic underestimation of the subhalo number densities and therefore the encounter rates. M. Barry et al. (2023) showed that increasing the particle resolution by a factor of 8 did not affect the number density of subhalos significantly.

While impact weighting of the encounter rates—where the contributions of individual encounters are weighted by their expected effects on a stream’s morphology—is crucial for predicting observable changes in a stream’s structure (D. Erkal & V. Belokurov 2015a; D. Erkal et al. 2016), here we focus solely on the increase in encounters due to the presence of the LMC’s subhalos and the MW’s response to the LMC. We have shown that  $\mathcal{I}(v_{\text{rad}})$  is similar across different mass bins up to a degree of nonconvergence in higher mass bins (Figure 7), indicating that the velocity field is not correlated with the subhalo masses. Additionally, we demonstrated that the LMC analog contributes a consistent fraction of subhalos across all mass decades globally, while the localized contributions can be significantly higher (Figure 9). This highlights that the impact weighting in the presence of the LMC subhalos on a stream morphology would be largely similar to the weighting in the absence of the LMC subhalos.

Moreover, this consistency indicates that our procedure of combining encounter rates across all mass decades is robust. In addition, it mitigates high jitter in the  $\mathcal{I}(v_{\text{rad}})$  integral, and given the uniform fractional contribution of subhalos from the LMC analog, it is straightforward to scale these results with  $n_{\text{sub}}$  for any given mass decade (M. Barry et al. 2023). This approach ensures that our analysis remains valid and reliable, regardless of the specific mass distribution of the subhalos.

#### 4.1. Encounter Rates of Synthetic Streams

We present statistically averaged encounter rates using the 5000 synthetic streams introduced in Section 2.3 as a function of three main properties: (1) galactocentric distance; (2) location on the sky, defined by the quadrant; and (3) angular momentum direction relative to the LMC analog’s angular momentum in m12b.

##### 4.1.1. Dependence on the Pericenter Distance and Sky Location

The encounter rates depend linearly on the number density of subhalos  $n_{\text{sub}}$  and on the velocity dispersion of subhalos in the stream-centric coordinates, both of which decrease as a function of the galactocentric distance. M. Barry et al. (2023) showed that the number density of subhalos is constant as a function of distance from the center out to 50 kpc at the present day; however, we found a decreasing trend in the number density around our integration time  $\approx 5$  Gyr before the present day. The top panel in Figure 11 shows the encounter rate per gigayear per stream length  $\ell_s$  and impact parameter  $b_{\text{max}}$  smoothed using the lowest regression (W. S. Cleveland & S. J. Devlin 1988) as a function of a stream’s pericentric distance in each quadrant (color-coded) defined in Figure 1, along with a spherically averaged encounter rate without the anisotropic boost ( $\tilde{\mu} = 0$ ) and the contributed subhalos (gray curve). The bottom panel shows the fractional changes in the rates relative to the spherically averaged rates. The overall number of encounters per gigayear ( $N_{\text{enc}}/\text{Gyr}$ ) decreases as a function of distance in all quadrants. The  $N_{\text{enc}}/\text{Gyr}$  values with  $\tilde{\mu} \neq 0$  (solid lines) consistently exhibit enhancements of 25%–70%, while the rates with  $\tilde{\mu} = 0$  (dashed lines) have a maximum enhancement of only about 25% from the changes in the number density of subhalos.

Q.I and Q.IV curves with  $\tilde{\mu} \neq 0$  show the highest increment in the rates, with increases of up to 50%–70% (bottom panel). The boost in Q.IV can be attributed to the LMC analog’s contributed subhalo increasing the number density of subhalos and changes in the effective  $\tilde{\gamma}$  (given by  $\tilde{\mu}/\sqrt{2}\sigma$ ). Q.I exhibits higher encounter rates due to the collective response and reflex motion. Q.III shows a relatively similar increase at larger distances owing to the contributed subhalos and the influence of the DM wake. Q.II has the lowest encounter rates, as none of the boosting effects are prominent there. On the other hand, m12i (not shown here) has no quadrant dependence, and the encounter rates with  $\tilde{\mu}$  are higher by 20% when compared with  $\tilde{\mu} = 0$ . We note that, even without an LMC analog,  $\tilde{\mu} = 0$  is generally nonzero; similarly, E. C. Cunningham et al. (2019) showed that velocity isotropy changes as a function of position on the sky.

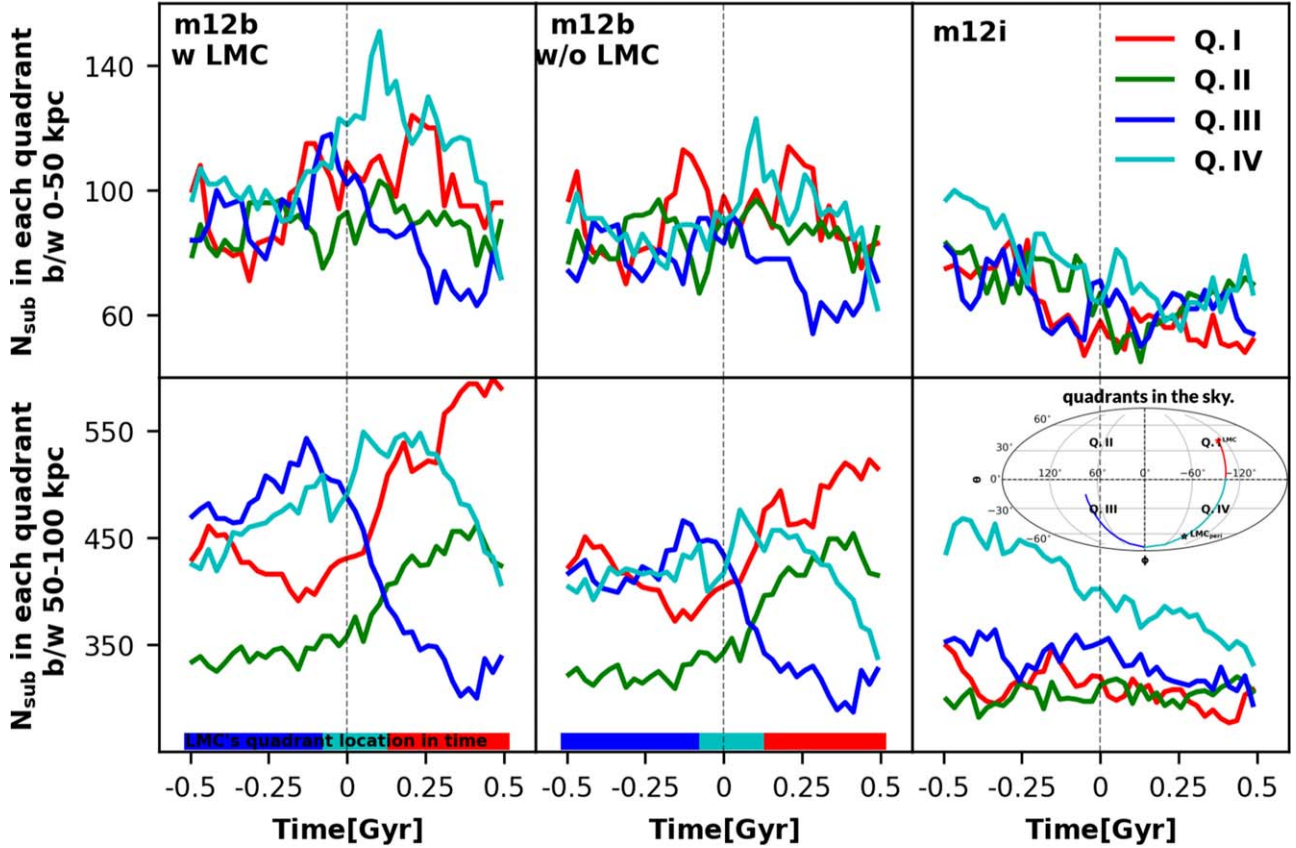


**Figure 10.** The number of subhalos in each quadrant (defined in Table 2) marked with different colors as a function of time within a time interval of  $\pm 0.5$  Gyr around the first pericenter of the LMC analog. The top row shows the subhalos in the inner halo (0–50 kpc), while the bottom row shows the subhalos in the outer halo (50–100 kpc). In m12b, we see large variations in the number of subhalos as a function of time. For example, prior to pericenter ( $-0.5$  Gyr onward), when the LMC analog is moving from Q.III to Q.IV, the number of subhalos sharply peaks in Q.II (opposite quadrant) in the middle panel. Looking at the left panel, in Q.IV the number of subhalos increases after pericenter, where the LMC analog moves. While in Q.III the number of subhalos decreases after pericenter as the LMC analog leaves Q.III. These changes are the result of the combination of the DM halo response (DM wake and collective response). The lower bar in the m12b panels marks the analog’s quadrant information with color in time.

#### 4.1.2. The LMC-analog Contribution to the Encounter Rates

In Figure 12, we plot the fractional enhancements in  $N_{\text{enc}}/\text{Gyr}$  resulting from the presence of the LMC analog’s contributed subhalos in m12b. These enhancements are computed by fractional change in the encounter rates with  $\tilde{\mu} \neq 0$  in the presence of the contributed subhalos and without these subhalos, using the lowest regression. Notably, the trends in fractional enhancements for encounter rates with  $\tilde{\mu} = 0$  show similar patterns.

The contributed subhalos have a more pronounced impact on the encounter rates in Q.III and Q.IV, yielding a substantial increase of nearly 15%–40% (Appendix C). This observation aligns with the findings from the first row of Figure 4. In contrast, Q.I and Q.II in the outer halo exhibit relatively lower enhancements, with values not exceeding 12%. Notably, Q.I in the outer halo showcases the least enhancement, and therefore the higher encounter rates seen at larger distances in Q.I in Figure 11 are primarily influenced by the reflex motion effects. We also found a higher localized boost of about 40% for another LMC-analog system in Appendix C, where the analog falls in closer to the present day (M. Barry et al. 2023).

In summary, our analysis highlights the crucial role of subhalo–stream kinematics, particularly the velocity distribution of subhalos, as a key factor in accurately predicting encounter rates. This results in a minimum overall enhancement of 25%. Moreover, we observe a notable dependence in the encounter rates on the location in the sky. Q.IV experiences

an additional enhancement of nearly 10%–40%, driven by the presence of contributed subhalos, while Q.I shows increased rates owing to the interplay of the collective response and reflex motion.

#### 4.1.3. Dependence on the Streams’ Orientation and Orbit

We categorize the synthetic streams as prograde or retrograde based on whether their orbital motion is in the same or opposite direction to that of the LMC analog, respectively. Among the 5000 synthetic streams, approximately 50% exhibit retrograde orbits relative to the LMC analog’s orbit, while the remaining 50% are in prograde orbits. Figure 13 plots the averaged encounter rates for streams in prograde (green) and retrograde (red) orbits as a function of a stream’s pericentric distance in each quadrant (marked in panels in rows 1 and 3). These rates are computed using robust regression (S. S. Wilks 1938; P. J. Huber 1973) in m12b with (solid lines) and without (dashed lines) contributed subhalos. The subpanels below each quadrant (rows 2 and 4) show  $\Delta_{\text{all}}$  as a function of a stream’s pericentric distance, which is the difference between the average encounter rates in each quadrant for each orbit type and the spherically averaged encounter rate for both orbit types, with and without contributed subhalos. The magenta bar in specific panels indicates the distance limits of the LMC analog within each quadrant during the calculation of encounter rates.

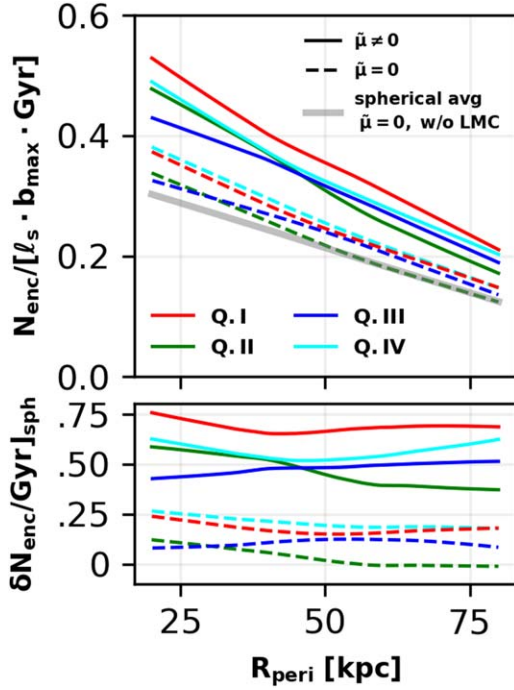


**Figure 11.** Estimated number of encounters per gigayear per stream length  $\ell_s$  and impact parameter  $b_{\max}$  in m12b with  $\tilde{\mu} \neq 0$  (solid) and  $\tilde{\mu} = 0$  (dashed). The rates are plotted as a function of a stream’s pericenter distance at  $T = 0$  Gyr in each quadrant (marked with different colors). The gray curve marks the encounter rates for m12b  $\tilde{\mu} = 0$  and without the contributed subhalos, as well as for m12i (rescaled to match the m12b halo mass), averaged over all quadrants. These curves are estimated using a lowess regression (W. S. Cleveland & S. J. Devlin 1988) from the 5000 synthetic streams. Streams in Q.I and Q.IV have the highest probability of encounters, as the LMC analog’s position in m12b at  $T = 0$  Gyr leads to a higher concentration of subhalos in Q.IV (at large distances), and the majority of the reflex motion and collective response effects are dominant in Q.I. Outer regions of Q.II have the lowest encounter rates of all, consistent with the spherically averaged rates marked by the gray curve. The second row plots the fractional changes in each encounter rate curve with respect to the spherically averaged rates.

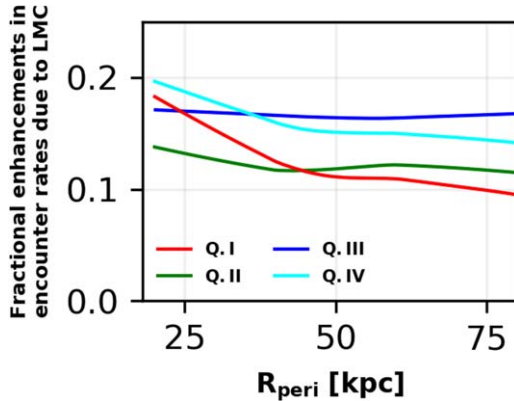


**Figure 12.** Fractional enhancements in the encounter rates due to the contributed subhalos from the LMC analog as a function of a stream’s pericentric distance in each quadrant (marked with different colors) for m12b. Streams exhibit a consistent increase of approximately 20% in encounter rates across all distance ranges in Q.III and inner regions of Q.IV owing to the contributed subhalos. In contrast, outer regions of Q.I show a smaller increment of  $\sim 10\%$  owing to contributed subhalos. Notably, Q.II has a constant increment of about 12% at larger distances, indicative of the presence of trailing contributed subhalos. These subhalos can boost the encounter rates through the halo by 15%.

In Q.I, the retrograde orbits with respect to the LMC analog consistently exhibit higher encounter rates than prograde orbits (approximately 0.02–0.08 more encounters or 50% higher than

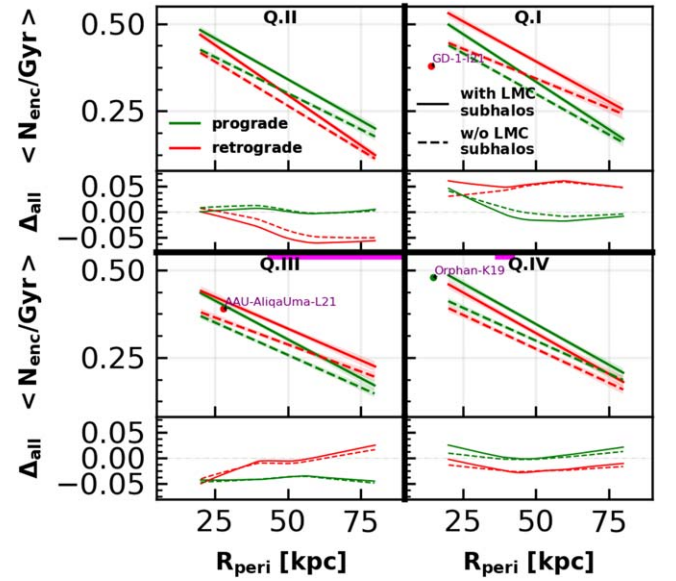


**Figure 13.** The average encounter rate (rows 1 and 3) is estimated using separate robust regressions (S. S. Wilks 1938; P. J. Huber 1973) for prograde (green) and retrograde (red) streams, taking into account the stream’s pericenter distance and sky position (quadrants marked on the panels). These calculations are performed in m12b with (solid) and without (dashed) contributed subhalos from the satellite. The difference with respect to the spherical average, denoted as  $\Delta_{\text{all}}$ , is also shown in rows 2 and 4 in each quadrant for each curve. The magenta bar marks the LMC analog’s distance in each quadrant within the time frame of the encounter rate calculation. Additionally, predicted encounter rates for the MW streams GD-1, Orphan, and AliqaUma, categorized by their orbit types, are also shown in their respective quadrants, plotted as a function of their present-day distance. We note that streams in retrograde orbits with respect to the LMC analog consistently exhibit higher encounter rates in Q.I (regions polar opposite to the analog’s trajectory).

the spherically averaged gray curve shown in Figure 11), regardless of the presence of the contributed subhalos. This is due to the relative bulk motion of subhalos, which aligns in the same direction as the retrograde stream orbits in Q.I, thereby increasing the likelihood of encounters.

In Q.IV, the prograde orbits in the outer regions have a higher number of encounters (approximately by  $0.02 \text{ Gyr}^{-1}$ ) owing to their motion aligning with that of the analog, which increases the likelihood of encountering subhalos, as the streams spend more time in close proximity to the contributed subhalos. Additionally, the presence of a transient DM wake can further contribute to the increased encounter rates for prograde orbits in the outer regions of Q.III.

In Q.II, retrograde streams have systematically lower rates than both the spherically averaged rates and prograde orbit rates. We think that this may be due to the fact that streams move between quadrants over the full integration time of 0.5 Gyr. The retrograde streams in Q.II preferentially enter via Q.III, where the relative velocity with subhalos from the LMC analog is high since most subhalos in that quadrant have a bulk velocity in the same sense as the analog’s orbit. This then produces an apparent decrement in retrograde encounters in Q.II. Conversely, streams that are moving prograde in Q.II at the end of the integration period came from Q.I, which is not strongly affected by the analog’s contributed subhalos. This would also produce the difference between the rates calculated with and without including the contributed subhalos that we also observe in Q.II. This quadrant serves as a reminder that the impact of the LMC on stream–subhalo encounters is not quite as simple as we would hope!

Furthermore, the encounter rates with  $\tilde{\mu} = 0$  (not depicted) show no discernible trends between different orbit types across any of the quadrants. However, the introduction of a nonzero  $\tilde{\mu}$  complicates the systematic perspective owing to the influence of the stream’s apparent motion on the anisotropic boost factor. Additionally, there is no observed dependence or correlation between a stream’s orbital eccentricity and encounter rates.

We annotate the GD-1 stream (C. J. Grillmair & O. Diona-  
tos 2006), the Orphan stream (C. J. Grillmair 2006; V. Belok-  
urov et al. 2007; S. E. Koposov et al. 2019), and the AliqaUma  
stream (T. S. Li et al. 2021b) in their respective quadrants and  
orbit types relative to the LMC analog. The trends observed in  
our synthetic streams generally align with those observed in the  
MW streams. The Orphan–Chenab stream closely interacts  
with the LMC and extends across both hemispheres of the MW  
(S. E. Koposov et al. 2023). Additionally, S. Lilleengen et al.  
(2023) have demonstrated the effects of the deforming MW  
halo on the proper motion and morphological structure of  
streams, making it challenging to differentiate between changes  
caused by subhalo–stream interactions and other influences.

#### 4.2. Encounter Rates of MW Streams

We have observed that synthetic streams around halos with  
an LMC analog display a diverse range of encounter rates,  
contingent on several factors: (1) the specific value of  $\tilde{\mu}$   
associated with the stream; (2) the stream location in the sky;  
and (3) the stream orbital rotation direction in relation to the  
LMC analog’s orbit. Notably, our findings demonstrated  
boosted encounter rates for orbits located in the northern  
hemisphere and in regions near and diametrically opposite to  
the LMC.

Expanding on our analysis, we now proceed to calculate  
encounter rates per gigayear per  $\ell_s$  and  $b_{\max}$  for all the MW  
streams within our simulation. We employ the same orbital  
integration methodology as employed for synthetic streams.  
However, for the MW streams, we substitute the initial  
conditions with the present-day phase-space coordinates of  
each stream in the MW. To establish these initial conditions,  
we utilize the median position and velocity of each stream  
track. We further adjust these conditions by applying a rotation  
that emulates the orientation of the actual streams relative to the  
real LMC as discussed in Section 2.3.

Our results are summarized in Table 3; we present the  
computed encounter rates ( $N_{\text{enc}}/\text{Gyr}$ ) in both m12b and m12i  
for the known MW streams (C. Mateu 2023). The table also  
includes the orbital properties of each stream, such as its  
present-day distance from the host galaxy ( $d$ ) and the sky  
quadrant ( $Q$ ) it occupies at  $T = 0$  Gyr in the context of m12b.  
The eccentricity of the orbit ( $e$ ) and its grade ( $G$ ) with respect  
to the LMC analog in m12b are also provided. The grade  
indicates whether the stream’s motion is prograde (in the same  
direction as the LMC analog’s orbit, denoted by “+”) or  
retrograde (opposite to the LMC analog’s orbit, denoted by  
“−”). These properties are calculated using the m12b potential  
models of DM halo and baryonic disks from A. Arora et al.  
(2022). It is crucial to emphasize that around 75% of the MW  
streams are situated within a radius of 20 kpc at  $T = 0$  Gyr.  
While interpreting these encounter rates, it is important to be  
cautious owing to the limited resolution in the inner regions.  
M. Barry et al. (2023) showed that the total subhalo population  
within a 50 kpc radius, 5 Gyr ago, was approximately twice as  
high for subhalos with  $M_{\text{sub}} \geq 10^6 M_{\odot}$  compared to the present-

day population. As a result, we can adjust our encounter rates  
by dividing them by a factor of 2. For example, M. Barry et al.  
(2023) estimated that the GD-1 stream, with a length of 15 kpc  
and an average impact parameter of 1.5 kpc, could experience  
approximately five encounters per gigayear using traditional  
symmetry and isotropy assumptions. With the inclusion of the  
LMC-induced subhalos, this rate increases twofold. In our  
analysis, our rescaled factor for present-day encounter rate for  
GD-1 with the same stream length and impact parameter is 3.5  
encounters per gigayear for m12i and 4.3 encounters per  
gigayear for m12b. These numbers are more or less similar  
because m12i has about 1.2 times fewer subhalos than m12b  
without the LMC-contributed subhalos. Given the location of  
GD-1 in the sky and distance from the center, we don’t expect  
any boosts in encounter rates due to the LMC, and our numbers  
are consistent with M. Barry et al. (2023) to the first order.

Among the MW streams analyzed, the Aquarius-W11 stream  
(M. E. K. Williams et al. 2011), Lethé-G09 (C. J. Grillm-  
air 2009), and Phlegethon-I21 (R. Ibata et al. 2021) in the inner  
halo (within 30 kpc) exhibit the highest encounter rates within  
the m12b simulation. Conversely, the Cetus-Y13 stream  
(W. Yam et al. 2013) has the highest encounter rate in the  
outer halo (at distances greater than 30 kpc). The streams C-7-  
I21 (R. Ibata et al. 2021), Ophiuchus-C20 (N. Caldwell et al.  
2020), and OmegaCen-I21 (R. Ibata et al. 2021) have the  
lowest encounter rates among the analyzed streams. These  
streams are located in the inner halo, orbiting within 7 kpc of  
the galactic center. Additionally, the Eridanus-M17 stream  
(G. C. Myeong et al. 2017), positioned at a distance of 100 kpc,  
exhibits the lowest encounter rates compared to other streams.

Overall, we observe consistent encounter rate trends for the  
MW streams across m12i and m12b, both with and without  $\tilde{\mu}$ .  
Streams situated beyond a present-day distance of 20 kpc in the  
m12b exhibit a clear dependence on location, with enhanced  
encounter rates in Q.II and Q.IV. Conversely, in m12i streams  
demonstrate no azimuthal dependence in the encounter rates.  
Incorporating  $\tilde{\mu}$  yields approximately a 30% boost for both  
m12b and m12i. The sense of rotation of the streams does not  
notably impact the encounter rates, mainly due to the proximity  
of these streams to the galactic center, while these effects are  
prominent for streams positioned in the outer halo regions.

## 5. Discussion: The Milky Way in Context

Currently, there are  $\approx 100$  observed streams in the MW.  
However, in the next decade we expect to discover more  
streams, especially in the outer halo, thanks to upcoming  
surveys such as the LSST (Ž. Ivezić et al. 2019). Furthermore,  
we will have a multidimensional view of the phase space and  
kinematics of the streams with unprecedented accuracy. As  
such, the search for disturbances from DM subhalos can be  
done systematically across large areas of the sky. With the  
insight from previous sections, we can anticipate specific areas  
in the MW sky where the likelihood of finding streams  
perturbed by subhalos is higher.

In Figure 14, we highlight the specific regions in the sky  
with an increased probability of detecting stream–subhalo  
interactions. These regions are identified by analyzing the sky  
positions of synthetic streams at  $T = 0$  Gyr in m12b, rotating  
them such that the LMC analog matches the real LMC location  
in the MW, considering the expected changes in the rates with  
and without the contributed subhalos. These regions are shaded  
manually by running a  $k$ -means clustering algorithm on the

**Table 3**  
Encounter Rates per Gigayear per Unit Stream Length (kpc) per Maximum Impact Parameter (kpc) of the MW Streams in m12b and m12i

Name	$d^a$ (kpc)	Q <sup>a</sup>	G	e	Enc. Rates	
					m12b	m12i
20.0-1-M18	20.0	III	...	0.3	0.4	0.4
300S-F18	20.6	I	+	0.6	0.4	0.3
AAU-AliqaUma-L21	27.9	III	...	0.5	0.4	0.4
AAU-ATLAS-L21	23.1	III	...	0.5	0.4	0.4
Acheron-G09	6.1	II	+	0.2	0.3	0.3
ACS-R21	18.7	II	+	0.1	0.5	0.3
Alpheus-G13	8.0	III	...	0.1	0.2	0.3
<b>Aquarius-W11</b>	8.1	III	+	0.6	0.8	0.4
C-19-I21	20.8	III	+	0.5	0.3	0.3
C-4-I21	10.1	II	...	1.0	0.4	0.3
C-5-I21	12.1	III	+	0.8	0.4	0.2
C-7-I21	4.0	III	+	0.4	0.1	0.2
C-8-I21	7.0	III	...	0.4	0.5	0.4
C-9-I21	12.1	III	...	0.1	0.4	0.3
Cetus-New-Y21	20.8	III	...	0.3	0.4	0.3
Cetus-Palca-T21	34.6	III	...	0.4	0.3	0.3
Cetus-Y13	35.3	III	...	0.2	0.4	0.4
Cocytos-G09	9.6	I	+	0.2	0.4	0.4
Corvus-M18	11.0	I	+	0.5	0.5	0.3
Elqui-S19	50.1	III	...	0.5	0.3	0.4
Eridanus-M17	100.0	III	...	0.6	0.1	0.1
<b>Gaia-1-I21</b>	8.2	I	...	0.6	0.6	0.3
Gaia-10-I21	18.4	I	...	0.1	0.5	0.3
Gaia-11-I21	12.0	II	...	0.9	0.4	0.4
Gaia-12-I21	18.2	III	+	0.3	0.3	0.3
Gaia-2-I21	10.8	III	...	0.2	0.4	0.4
<b>Gaia-3-M18</b>	12.9	I	+	0.6	0.6	0.3
Gaia-4-M18	14.5	I	+	0.5	0.6	0.2
Gaia-5-M18	25.5	I	+	0.2	0.5	0.3
<b>Gaia-6-I21</b>	10.4	I	...	0.2	0.5	0.2
Gaia-7-I21	8.7	I	+	0.4	0.4	0.2
Gaia-8-I21	8.6	I	...	0.3	0.4	0.2
Gaia-9-I21	9.4	II	+	0.9	0.4	0.4
GD-1-I21	14.2	I	...	0.1	0.4	0.3
Gunnthra-I21	6.3	III	+	0.4	0.2	0.3
Hermus-G14	17.3	II	+	0.5	0.6	0.3
Hrid-I21	8.0	II	...	0.9	0.6	0.4
Hyllus-G14	17.4	II	+	0.5	0.6	0.4
Indus-S19	13.6	III	+	0.2	0.4	0.4
Jet-F22	34.0	IV	...	0.7	0.4	0.3
Jhelum-a-B19	11.3	III	+	0.6	0.4	0.5
Jhelum-b-B19	11.4	III	+	0.6	0.4	0.5
Kshir-I21	14.8	II	...	0.6	0.4	0.3
Kwando-G17	22.9	III	...	0.2	0.4	0.3
Leiptr-I21	13.7	IV	+	0.7	0.4	0.3
Lethe-G09	13.3	I	+	0.2	0.5	0.3
LMS1-Y20	12.4	I	+	0.6	0.4	0.2
M2-I21	9.8	III	+	0.9	0.3	0.3
M30-S20	7.0	III	...	0.3	0.4	0.3
M5-G19 <sup>b</sup>	13.7	I	...	–	0.7	0.4
M68-P19	8.9	I	+	0.4	0.4	0.4
M92-I21	10.3	II	...	0.6	0.3	0.3
Molonglo-G17	21.0	III	...	0.2	0.4	0.3
Monoceros-R21	18.2	II	+	0.1	0.4	0.3
Murrumbidgee-G17	21.0	III	...	0.3	0.4	0.3
NGC1261-I21	21.4	IV	+	0.9	0.5	0.4
NGC1851-I21	17.8	IV	+	0.7	0.3	0.3
NGC2298-I21	17.4	IV	+	0.9	0.4	0.4
<b>NGC288-I21</b>	13.7	III	+	0.6	0.6	0.2
NGC3201-P21	11.0	IV	+	0.6	0.5	0.3
<b>NGC5466-G06</b>	17.5	I	+	0.2	0.5	0.2
<b>NGC6362-S20</b>	5.0	IV	...	0.7	0.6	0.2

**Table 3**  
(Continued)

Name	$d^a$ (kpc)	Q <sup>a</sup>	G	e	Enc. Rates	
					m12b	m12i
NGC6397-I21	5.9	III	...	0.5	0.2	0.1
OmegaCen-I21	7.0	IV	...	0.4	0.1	0.1
<b>Ophiuchus-C20</b>	4.3	I	...	0.8	0.2	0.0
Orinoco-G17	22.2	III	...	0.2	0.4	0.3
Orphan-K19	14.8	IV	+	0.2	0.5	0.3
Pal13-S20	24.8	III	...	0.6	0.4	0.3
Pal15-M17	31.6	I	+	0.3	0.4	0.2
Pal5-PW19 <sup>b</sup>	16.6	I	...	–	0.7	0.6
Palca-S18	37.5	III	...	0.2	0.3	0.3
<b>Parallel-W18</b>	16.9	I	+	0.4	0.5	0.2
Pegasus-P19	18.6	II	...	0.7	0.6	0.3
<b>Perpendicular-W18</b>	17.5	I	+	0.2	0.6	0.2
Phlegethon-I21	6.7	III	+	0.6	0.7	0.4
Phoenix-S19	18.5	III	...	0.2	0.4	0.4
PS1-A-B16	13.6	III	...	0.1	0.4	0.3
<b>PS1-B-B16</b>	18.7	IV	+	0.5	0.5	0.3
PS1-C-B16	17.5	III	...	0.7	0.6	0.4
PS1-D-B16	28.1	IV	+	0.5	0.4	0.3
<b>PS1-E-B16</b>	17.6	II	+	0.2	0.6	0.2
Ravi-S18	19.7	III	...	0.8	0.4	0.4
Sagittarius-A20	8.3	III	...	0.9	0.3	0.4
Sangarius-G17	27.1	IV	+	0.4	0.4	0.3
Scamander-G17	26.1	I	+	0.4	0.4	0.3
Slidr-I21	9.4	IV	...	0.5	0.4	0.3
Styx-G09	42.3	I	+	0.3	0.3	0.1
Svol-I21	7.8	II	+	0.3	0.3	0.4
<b>Sylgr-I21</b>	8.7	I	...	0.3	0.5	0.2
Tri-Pis-B12	31.4	III	...	0.4	0.4	0.3
TucanaIII-S19	23.1	III	...	0.7	0.4	0.5
Turbio-S18	17.6	III	...	0.5	0.4	0.3
Turraburra-S19	32.9	III	...	0.7	0.3	0.3
Vid-I21	26.3	III	...	0.3	0.3	0.4
Wambelong-S18	19.5	IV	+	0.6	0.4	0.3
Willka_Yaku-S18	34.4	IV	...	0.4	0.2	0.2
<b>Ylgr-I21</b>	11.9	I	...	0.8	0.5	0.2

**Notes.** Note that M. Barry et al. (2023) demonstrated that the total subhalo population within a 50 kpc radius 5 Gyr ago was nearly twice as high as the present-day population. Therefore, our rates can be extrapolated to the present day by appropriately scaling them down by a factor of 2.  $d$ : distance of the stream from the MW. Q: Quadrant in the sky. G: orbit's motion, prograde (+) or retrograde (–) with respect to the LMC-analog orbit in m12b.  $e$ : eccentricity of the stream orbit in m12b. Streams with encounter rate ratios of at least 2 between m12b and m12i are highlighted in bold.

<sup>a</sup> Computed at  $T = 0$  Gyr.

<sup>b</sup> Missing proper-motion information in galstreams.

stream locations (J. MacQueen 1967), dividing the stream positions in the Galactocentric coordinates into three distinct groups: one group for the background, another for the reflex motion, and a third for the LMC subhalos and DM wake categories, while also removing any outliers.

The red shaded region is the polar opposite region to the LMC, where the dominant effect on stream–subhalo interactions is the reflex motion response, in both position and velocity. The purple shaded region indicates a higher subhalo density due to the presence of LMC subhalos in the leading debris and the LMC itself. Streams located within these shaded regions are expected to have a higher likelihood of encounters with subhalos. Our estimates based on Section 4 suggest an

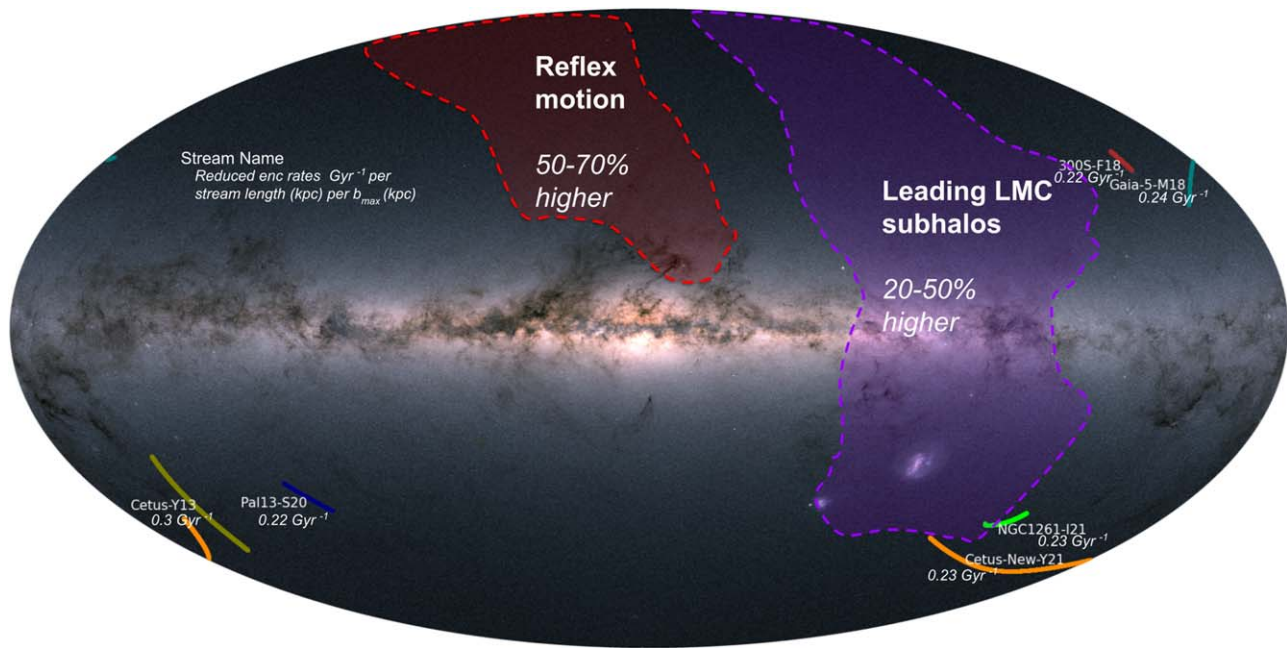


**Figure 14.** Regions with the highest encounter rate enhancements due to the LMC, superimposed on the stellar flux map from Gaia DR2 (C. Gaia et al. 2018). Shaded regions on the map indicate higher overall probabilities of encounter rates, which have been determined using the top 1% synthetic streams in m12b, rotated to align with the MW–LMC orientation at the present day. To aid visualization, the synthetic streams have been color-coded using a  $k$ -means clustering algorithm (J. MacQueen 1967), and shaded regions have been manually drawn. Also marked are the MW streams with the highest encounter rate enhancements located at distances greater than 20 kpc, along with their reduced (by a factor of 2) rates per 10 kpc stream length and impact parameter in m12b. Streams within the shaded regions labeled as reflex motion (red) and subhalos brought in by the LMC (purple) are anticipated to have a higher probability of subhalo–stream interactions by as much as 50%–70% and 20%–50%, respectively, compared to the spherically averaged rates without accounting for the LMC-contributed subhalos.

enhancement ranging from 50% to 70% (depending on the stream’s orbital orientation; Figure 13) in the reflex motion region (red shaded area) and from 20% to 50% in the region influenced by the leading LMC subhalos (see Figures 11 and 12) (purple shaded area) with respect to the spherically averaged rates without accounting for the LMC-contributed subhalos.

Additionally, we include the MW streams orbiting beyond 20 kpc from the galactic center, with encounter rates greater than the 90th percentile limit (4.4 encounters per gigayear) based on our calculations in m12b (see Table 3). We also list their corrected-for-present-day (reduced by a factor of 2) encounter rates per stream length of 10 kpc and impact parameter.

We predict that streams such as NGC1261-I21 (R. Ibata et al. 2021), Scamander-G17 (C. J. Grillmair 2017), Sangarius-G17 (C. J. Grillmair 2017), AAU-AliqaUma-L21 (T. S. Li et al. 2021b), Cetus-Y13 (W. Yam et al. 2013), and Gaia-5-M18 (K. Malhan & R. A. Ibata 2018) have the highest likelihood of subhalo encounters in the outer regions of the stellar halo.

These predictions can be valuable for observing strategies aimed at detecting spurs, kinks, and gaps in streams during future surveys, particularly in the outer regions of the halo. Surveys such as the Vera Rubin Observatory (Ž. Ivezić et al. 2019), Nancy Grace Roman Space Telescope (D. Spergel et al. 2013, 2015), DESI (C. DESI et al. 2016), WEAVE (G. Dalton et al. 2012), 4MOST (R. S. De Jong et al. 2019), and Subaru PFS (M. Takada et al. 2014), among others, can prioritize regions in the sky where streams are more likely to have encounters with subhalos. It is important to note that caution is required when interpreting these values as calibration benchmarks for specific stream regions. Instead, they offer insight into

the potential systematic uncertainties that can arise from departures from equilibrium assumptions in these measurements.

## 6. Conclusions

In this paper, we have investigated the impact of a massive satellite on the encounter rates between stellar streams and DM subhalos. Leveraging two representative systems from the FIRE-2 hydrodynamical zoom-in simulations—one featuring an LMC analog and the other lacking any massive satellite—we address two key questions. First, we evaluated how the LMC analog’s subhalo population contributes to enhancing encounter rates with host stellar streams, building on the work of M. Barry et al. (2023) and using the same simulations. Second, we investigated how the host halo’s response influences encounter rates galaxy-wide.

Our findings indicate a general decrease in encounter rates with increasing pericentric distance, independent of the eccentricity of a stream’s orbit. The presence of a massive satellite, such as the LMC analog, introduces an anisotropic boost, resulting in varying encounter rates for streams across different regions of the sky relative to the satellite. Key factors influencing these asymmetric effects are ranked as follows:

1. *Mean radial motion.* The mean radial motion of subhalos with respect to streams, represented by  $\bar{\mu}$ , consistently enhances encounter rates by at least 30% even in systems without the LMC analog. Under the influence of an LMC analog, localized boosts can jump up to 70% as observed in Q.I, compared to the spherically symmetric and  $\bar{\mu} = 0$  rates (Figure 11).
2. *Contribution from the LMC-analog subhalos.* The LMC analog brings its own set of subhalos with unique phase-space orbits, as depicted in Figure 4. These subhalos can

boost the encounter rate up to 10%–40% in Q.III and Q.IV, aligned with the LMC analog’s motion (Figures 12 and 17). This boost may be much higher in the MW today (Appendix C). M. Barry et al. (2023) showed that the number density can be boosted up to a factor of 2 owing to the LMC-mass satellites.

3. *Orbital alignment.* Streams in retrograde orbits with respect to the LMC analog, particularly located in the outer halo and the opposite hemisphere from the analog, exhibit enhanced rates up to 30%, with the most substantial boosts occurring in Q.I compared to prograde streams (Figure 13).

In conclusion, our investigations reveal that streams situated in proximity to the LMC and in regions opposite to it are more likely to interact with subhalos, potentially leading to detectable morphological changes. Building on this insight, we have identified regions within the MW–LMC celestial sphere likely to display signatures of stream–subhalo interactions, as depicted in Figure 14. Detecting such signatures and constraining the perturbing subhalo masses will offer valuable insights into allowed DM models with specific subhalo mass scales. Furthermore, our results emphasize the complexities introduced by the presence of a massive satellite such as the LMC, suggesting that the MW might not be an ideal laboratory for constraining the subhalo mass function, due to the need to consider departures from the equilibrium assumptions. In this context, finding extragalactic streams orbiting in galaxies in a state of dynamical equilibrium presents promising opportunities for precise constraints on the DM subhalo mass function. With upcoming missions like the Roman Space Telescope (D. Spergel et al. 2013, 2015), we anticipate the detection of such streams in other galaxies (S. Pearson et al. 2022; C. Aganze et al. 2023), enhancing our ability to derive valuable insights into the nature of DM.

### Acknowledgments

The authors thank the anonymous referee, Denis Erkal, Gurtina Besla, Kathryn V. Johnston, and Adrian Price-Whelan for valuable discussions that shaped this paper.

A.A. and R.E.S. acknowledge support from the Research Corporation through the Scialog Fellows program on Time Domain Astronomy, from NSF grant AST-2007232, and from NASA grant 19-ATP19-0068. R.E.S. is supported in part by a Sloan Fellowship. E.C.C. acknowledges support from NASA through the NASA Hubble Fellowship Program grant HST-HF2-51502 awarded by the Space Telescope Science Institute, which is operated by the Association of Universities for Research in Astronomy, Inc., for NASA, under contract NAS5-26555. A.W. and M.B. received support from NSF via CAREER award AST-2045928 and grant AST-2107772, NASA ATP grant 80NSSC20K0513, and HST grants AR-15809, GO-15902, and GO-16273 from STScI.

This research is part of the Frontera computing project at the Texas Advanced Computing Center (TACC). Frontera is made possible by the National Science Foundation award OAC-1818253. Simulations in this project were run using Early Science Allocation 1923870 and analyzed using computing resources supported by the Scientific Computing Core at the Flatiron Institute. This work used additional computational resources of the University of Texas at Austin and TACC, the

NASA Advanced Supercomputing (NAS) Division and the NASA Center for Climate Simulation (NCCS), and the Extreme Science and Engineering Discovery Environment (XSEDE), which is supported by National Science Foundation grant No. OCI-1053575.

A.A. would like to express sincere gratitude to ChatGPT for its invaluable language assistance (and for writing its own acknowledgment) and to OpenAI for providing the platform and technology.

*Software:* Astropy (Astropy Collaboration et al. 2013, 2018, 2022), IPython (F. Perez & B. E. Granger 2007), Matplotlib (J. D. Hunter 2007), Numpy (C. R. Harris et al. 2020), Pandas (W. McKinney 2010), Scipy (P. Virtanen et al. 2020), Healpy (A. Zonca et al. 2019), `consistent-trees` (P. S. Behroozi et al. 2012b), `rockstar` (P. S. Behroozi et al. 2012a), `halo_analysis` (A. Wetzel & S. Garrison-Kimmel 2020b), `gizmo_analysis` (A. Wetzel & S. Garrison-Kimmel 2020a), `galstreams` (C. Mateu 2023), AGAMA (E. Vasiliev 2019), CMasher (E. van der Velden 2020).

### Appendix A

#### Rotational Transformation of the LMC-analog Location to the Real LMC

The LMC analog in m12b is located at  $\mathbf{x}_{\text{analog}} = (-23.3, -26.6, 13.7)$  kpc at  $T_{\text{peri}}$  in the principal axis frame. However, we establish as the “rotated axes” the ones that align the position unit vector of the LMC analog in m12b at its first pericentric passage with the position unit vector of the *real* LMC in the MW at its first pericentric passage, located at  $\mathbf{x}_{\text{LMC}} = (2.3, -20.2, -41.1)$  kpc, based on the orbits presented in N. Garavito-Camargo et al. (2019).

We compute the rotation matrix  $R_{\text{LMC}}$  using Rodrigues’s rotation formula such that  $\hat{\mathbf{x}}_{\text{analog}} = R_{\text{LMC}}^T \hat{\mathbf{x}}_{\text{LMC}}$  and

$$R_{\text{LMC}} = I + [v]_{\times} + \frac{[v]_{\times}^2}{1 + \hat{\mathbf{x}}_{\text{LMC}} \cdot \hat{\mathbf{x}}_{\text{analog}}}, \quad (\text{A1})$$

where  $I$  is the identity,  $v$  is given by  $\hat{\mathbf{x}}_{\text{LMC}} \times \hat{\mathbf{x}}_{\text{analog}}$ , and  $[v]_{\times}$  is the skew-symmetric cross-product of  $v$ .

For the specific values of  $\mathbf{x}_{\text{LMC}} = (2.3, -20.2, -41.1)$  kpc and the analog in m12b  $\mathbf{x}_{\text{analog}} = (-23.3, -26.6, 13.7)$  kpc, the rotation matrix is given by

$$R_{\text{LMC}} = \begin{bmatrix} 0.60508764 & -0.1328807 & 0.78499151 \\ -0.74603358 & 0.24968852 & 0.6173245 \\ -0.27803387 & -0.95916545 & 0.05194997 \end{bmatrix}. \quad (\text{A2})$$

### Appendix B

#### Gaussianity Analysis of Subhalos’ Radial Velocity Distributions

In this appendix, we investigate the Gaussianity assumption underlying the probability density function (pdf) for the subhalos’ radial velocity  $P(\tilde{v}_r)$  in stream-centric coordinates. This assumption plays a crucial role in deriving an analytical model for the subhalo–stream encounter rates, as expressed in Equation (10).

Figure 15 shows the anisotropic boost factor,  $f(\tilde{\gamma})$  from Equation (10), as a function of  $\tilde{\gamma}$ . The boost factor approaches 0 for a large positive mean velocity (i.e., all the subhalos

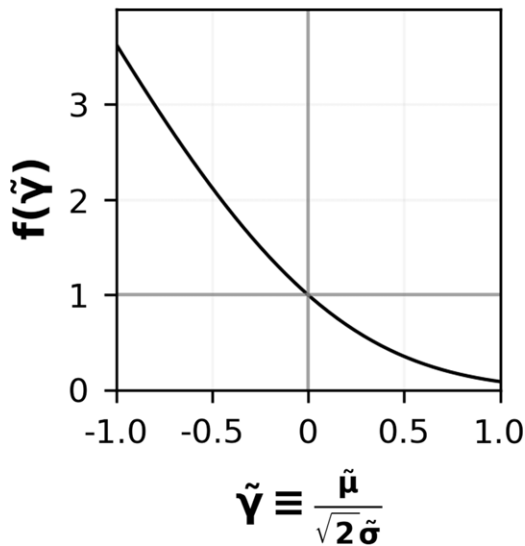


**Figure 15.** The anisotropic boost factor  $f(\tilde{\gamma})$  in Equation (10) that is dependent on the Gaussian parameters of the cylindrical radial velocity distribution of subhalos with respect to a stream as a function of a typical  $\tilde{\gamma}$ , i.e., is a function of mean radial velocity ( $\tilde{\mu}$ ) and velocity dispersion ( $\tilde{\sigma}$ ) of subhalos in the stream-centric coordinates. Theoretically the factor converges to 0 with  $\tilde{\gamma} \gg 0$  and diverges to infinity for  $\tilde{\gamma} \ll 0$ . Parameter  $f(\tilde{\gamma})$  strongly depends on  $\tilde{\mu}$  and  $\tilde{\sigma}$ , and hence assuming  $\tilde{\mu} = 0$  can bias the estimates of encounter rates.

moving away from the stream) and diverges to infinity for a large negative mean velocity (all the subhalos approaching the stream in the finite time interval). In the MW, the velocity dispersion of the outer halo is of order  $\sigma = 100 \text{ km s}^{-1}$  (A. J. Deason et al. 2012; J. G. Cohen et al. 2017), and the expected mean velocity is  $\tilde{\mu} = 35 \text{ km s}^{-1}$  (D. Erkal et al. 2019; M. S. Petersen & J. Peñarrubia 2020). For an MW stream in a circular orbit the anisotropic boost factor will scale the encounter rates to 1.75 or 0.5 depending on whether  $\tilde{\mu}$  is locally negative or positive in the stream’s frame. Notably, a negative  $\tilde{\mu}$  value leads to a substantial rate enhancement, and a positive  $\tilde{\mu}$  leads to a reduction. For instance, a  $\tilde{\gamma}$  of  $-0.25$  results in a 50% boost in encounter rates, while a  $+0.25$  value leads to a 35% decrease. For halos with no massive satellites, M. Barry et al. (2023) showed that in the galactocentric frame at the present day the orbital velocity vectors of subhalos are generally isotropic at all distances.

We examine the validity of assuming a Gaussian distribution  $J_{\text{gauss}}(\tilde{\mu}, \tilde{\sigma})$  for  $P(\tilde{v}_R)$ . It is noteworthy that the pdfs subjected to analysis in this section exclusively concern subhalos positioned around streams, in accordance with the description provided in Section 2.5 within the context of the m12b at  $T = 0 \text{ Gyr}$ . This specific choice is motivated by the fact that the LMC analog’s first pericentric passage induces significant perturbations on the Gaussianity assumption, due to its pronounced dipolar moment (E. C. Cunningham et al. 2020; M. S. Petersen & J. Peñarrubia 2020).

The left panel of Figure 16 shows  $P(\tilde{v}_R)$  (solid lines) and their corresponding Gaussian fits (dashed lines) for a representative set of MW streams (varied colors). Notably, the means of different pdfs and their fits display similar trends. It is important to note that this mean value can shift, toward either more negative or more positive values, thereby leading to the conditions  $f(\tilde{\gamma}) \geq 1$  or  $f(\tilde{\gamma}) \leq 1$ , respectively. This shift’s potential influence on the scaling factor behavior is highlighted. The alignment between Gaussian distributions and actual pdfs visually confirms the Gaussian fitting assumption.

For a quantitative analysis, we perform numerical integration for the 5000 synthetic streams at  $T = 0 \text{ Gyr}$  in m12b, assuming a Gaussian approximation (see Equation (10)), hereafter labeled as  $\mathcal{I}_{\text{gauss}}$ , and conducting the exact numerical integral ( $\mathcal{I}_{\text{num}}(\tilde{v}_R)$ ) without any assumption (see Equation (7) in Section 2.5). We compute the residual as  $\mathcal{I}_{\text{gauss}}/\mathcal{I}_{\text{num}} - 1$  to assess the errors introduced by the approximation.

The bottom panel of Figure 16 shows the resulting residual distribution for the 5000 synthetic streams in m12b at  $T = 0 \text{ Gyr}$ . The dashed line represents the 50th quantile, and the dashed-dotted lines mark the 16th and 84th quantiles. The majority of errors fall within 10% of the expected values, with the mean and standard deviation of the distribution being 0.01 and 0.08, respectively. This translates to an average error of 1% with a deviation of 8%. We also note that the majority of higher errors ( $\geq 10\%$ ) occur for streams close to the galactic center and the disk stemming from the low subhalo population. These results highlight the accuracy of the Gaussian approximation method, especially compared to other assumptions used in such analysis.

For a qualitative evaluation, we test the Gaussian assumption using the Shapiro–Wilk test (S. S. Shapiro & M. B. Wilk 1965) on the pdfs of 5000 synthetic streams. This statistical test evaluates the null hypothesis of Gaussian distribution for each  $P(\tilde{v}_r)$ .

The right panel of Figure 16 depicts a histogram of computed  $p$ -values (null hypothesis confidence) from the Shapiro–Wilk test. The red shaded region identifies the 0.05 significance threshold, marking  $p$ -values below which the null hypothesis is rejected. Among the analyzed distributions, 2143 exhibit  $p$ -values below 0.05 (non-Gaussian behavior), while 2857 distributions show  $p$ -values above 0.05 (green region), reinforcing the Gaussian assumption, as over 50% of the distributions have  $p$ -values in the green region.

Remarkably, the  $p$ -value counts demonstrate a logarithmic decrease, highlighting a gradual transition from non-Gaussian to Gaussian behavior in the pdfs. This observation further endorses the Gaussian approximation’s appropriateness for the pdfs. While the numerical 1D integrals are efficient, the assumption of Gaussianity remains valid and imposes no significant constraints compared to other approximations commonly employed in such analyses.

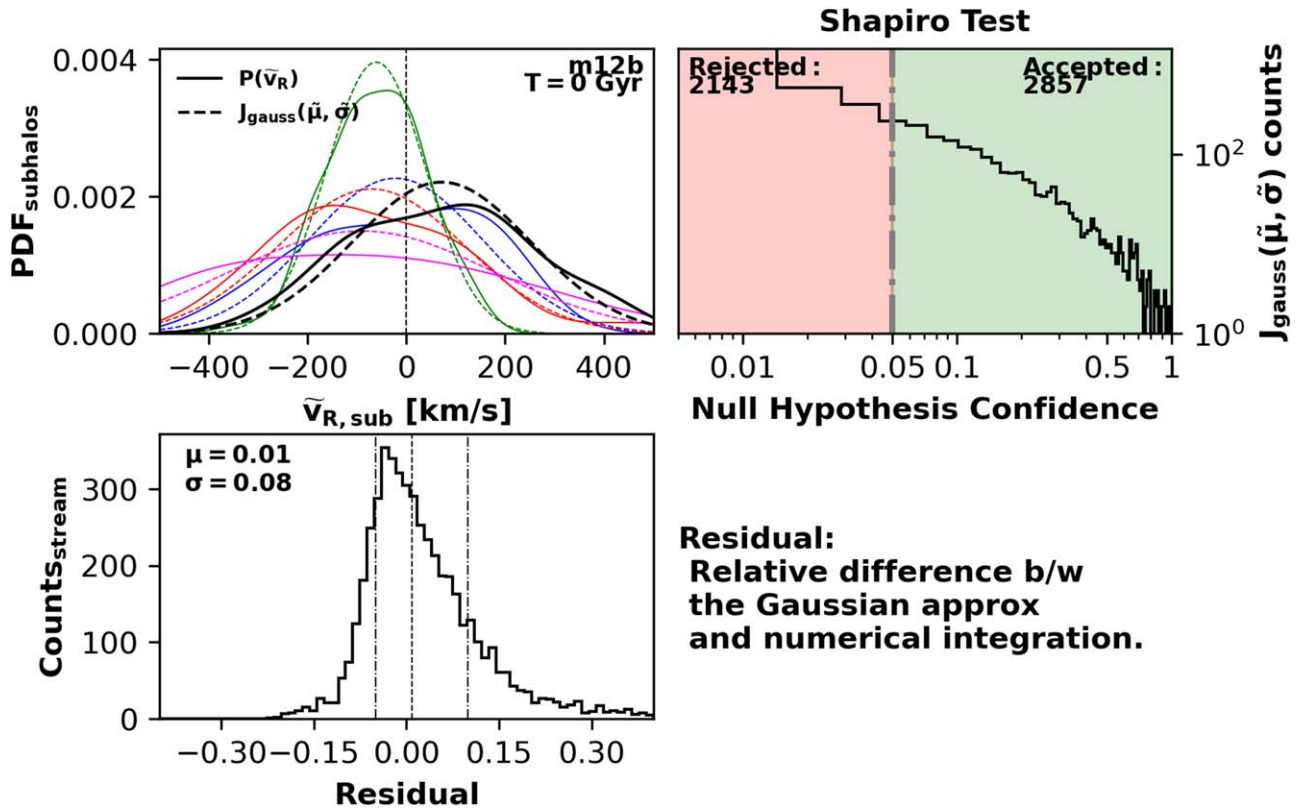


**Figure 16.** Left: pdf of the cylindrical radial velocity  $P(\tilde{v}_R)$  in stream-centric coordinates (solid lines), along with corresponding Gaussian distribution fits  $J_{\text{gauss}}(\tilde{\mu}, \tilde{\sigma})$  (dashed lines) for a representative sample of MW stream orbits injected in m12b, illustrated with different colors at  $T = 0$  Gyr. This comparison visually attests to the adequacy of Gaussian approximation. Right: histogram of computed  $p$ -values obtained through the Shapiro–Wilk test (S. S. Shapiro & M. B. Wilk 1965), which assesses the null hypothesis of normal distribution. This is applied to the pdf of subhalos’ cylindrical radial velocity  $P(\tilde{v}_R)$  in stream-centric coordinates for the 5000 synthetic stream orbits in m12b at  $T = 0$  Gyr. The red shaded region indicates the 0.05 significance threshold, below which the null hypothesis is rejected. Conversely, green shaded regions denote acceptance. Over 50% of pdfs analyzed follow Gaussianity from the accepted number of samples. Bottom: distribution of residuals calculated between the Gaussian approximation of Equation (10) and the exact numerical integration (Equation (9)) without any assumptions on the cylindrical radial velocities of subhalos’ distribution in stream-centric coordinates. Residuals are computed at  $T = 0$  Gyr for the 5000 synthetic streams in m12b. The dashed line represents the 50th quantile, and dashed–dotted lines mark the 16th and 84th quantiles. Most errors in assuming the approximation are within 10%.

### Appendix C

#### Encounter Rates in Another LMC Analog (m12c)

In this appendix, we repeat our analysis from Section 4.1. We achieve this by injecting and integrating 5000 synthetic stream orbits, as described in Section 2.3 in the context of m12c, which has *another* LMC analog, with the first pericentric passage at about 1 Gyr before the present day, at a much closer distance of 18 kpc from the host center. Following M. Barry et al. (2023), we assume  $T = 0$  Gyr (first pericentric passage), when the LMC analog is 50 kpc away from the center. The LMC analog’s orbit largely lies in the disk plane until  $T = 0.2$  Gyr. During this time, the analog starts in Q.IV and moves inward with the first pericenter ( $T = 0$  Gyr) into Q.I. The actual pericenter occurs in Q.II at  $T = 0.15$  Gyr. We integrate our synthetic stream orbits from  $-0.4$  to  $0$  Gyr (in contrast to integrating from  $-0.4$  to  $0.1$  Gyr in the m12b case) and do not anticipate significant north–south asymmetry (collective response) or the emergence of reflex motion during this period, given that the LMC remains in the galactic disk plane.

The left panel of Figure 17 shows the average encounter rates of synthetic streams as a function of their pericentric distances in different quadrants (color-coded) within the context of m12c. A comparison with the encounter rates in

m12b (Figure 11) reveals an overall reduction by a factor of 1.6. This decrease is due to a higher number of subhalos in the MW 5 Gyr before the present day compared to 1 Gyr ago (see Figure 4 in M. Barry et al. 2023). Notably, Q.I and Q.IV exhibit the highest encounter rates, aligning with the LMC analog’s orbit and the expected DM wake. Q.II also displays some increased rates in the inner regions.

The right panel of Figure 17 plots the fractional enhancements in  $N_{\text{enc}}/\text{Gyr}$  due to the contributed subhalos in m12c. Even though both the LMC analogs (in m12c and m12b) start with the same number of subhalos, the overall enhancements in m12c are higher than those in m12b (Figure 12), due to the decreased MW subhalo population at later times. Q.I and Q.II exhibit a consistent enhancement of 30% or more in the inner regions, due to the leading arm of the contributed subhalos tracing the analog’s future orbit, while Q.I and Q.IV both experience over 20% increase in the outer halo. The total fractional enhancement for the real LMC is more accurate for m12c; given the LMC analog’s proximity to the present day, it is important to note that the quadrant and distance dependencies are highly sensitive to the orbit and pericentric distance, making m12b more suitable for predicting regions of enhancements from the real LMC.

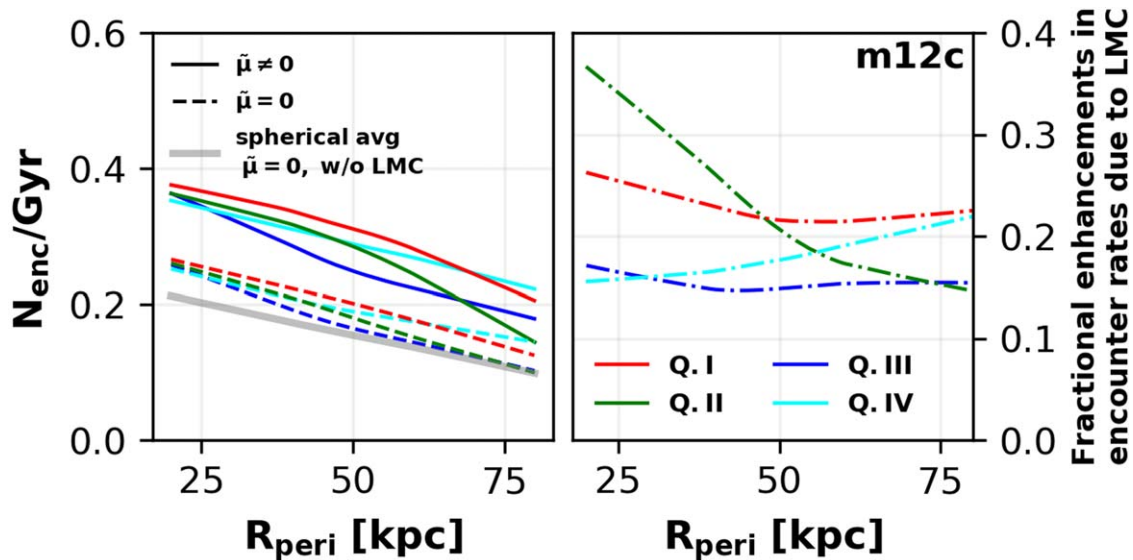


**Figure 17.** Encounter rates in Section 4.1 for m12c, assuming  $T = 0$  Gyr when the LMC analog is at a distance of 50 kpc from the host center. Left: estimated number of encounters per gigayear per unit stream length  $\ell_s$  and maximum impact parameter  $b_{\max}$  in m12c with  $\tilde{\mu}$  (solid) and without  $\tilde{\mu}$  (dashed) plotted as a function of the stream's pericenter distance at  $T = 0$  Gyr and four quadrants (marked by colors; compare to Figure 11). The gray line represents the range of encounter rates for m12c with  $\tilde{\mu} = 0$  and without contributed subhalos, averaged over all quadrants. The highest encounter rates occur in Q.I and Q.IV (where the LMC analog orbits in the integration time frame). Right: fractional enhancements in the encounter rates due to contributed subhalos from the LMC analog for m12c (compare to Figure 12). Q.I and Q.IV exhibit a consistent 20% increase in the encounter rates in the outer halo due to a higher subhalo density around the analog. In contrast, Q.II shows the highest enhancements in the inner regions (up to 35%), due to the leading arm of the contributed subhalos.

### ORCID iDs

Arpit Arora <https://orcid.org/0000-0002-8354-7356>  
 Nicolás Garavito-Camargo <https://orcid.org/0000-0001-7107-1744>  
 Robyn E. Sanderson <https://orcid.org/0000-0003-3939-3297>  
 Emily C. Cunningham <https://orcid.org/0000-0002-6993-0826>  
 Andrew Wetzel <https://orcid.org/0000-0003-0603-8942>  
 Nondh Panithanpaisal <https://orcid.org/0000-0001-5214-8822>  
 Megan Barry <https://orcid.org/0000-0002-1176-0078>

### References

Aganze, C., Pearson, S., Starkenburg, T., et al. 2024, *ApJ*, 962, 151  
 Arora, A., Sanderson, R. E., Panithanpaisal, N., et al. 2022, *ApJ*, 939, 2  
 Arora, A., Sanderson, R., Regan, C., et al. 2024, arXiv:2407.12932  
 Astropy Collaboration, Price-Whelan, A. M., Lim, P. L., et al. 2022, *ApJ*, 935, 167  
 Astropy Collaboration, Price-Whelan, A. M., Sipőcz, B. M., et al. 2018, *AJ*, 156, 123  
 Astropy Collaboration, Robitaille, T. P., Tollerud, E. J., et al. 2013, *A&A*, 558, A33  
 Banik, N., Bovy, J., Bertone, G., Erkal, D., & De Boer, T. 2021a, *JCAP*, 2021, 043  
 Banik, N., Bovy, J., Bertone, G., Erkal, D., & De Boer, T. 2021b, *MNRAS*, 502, 2364  
 Barry, M., Wetzel, A., Chapman, S., et al. 2023, *MNRAS*, 523, 428  
 Behroozi, P. S., Wechsler, R. H., & Wu, H.-Y. 2012a, *ApJ*, 762, 109  
 Behroozi, P. S., Wechsler, R. H., Wu, H.-Y., et al. 2012b, *ApJ*, 763, 18  
 Belokurov, V., Evans, N. W., Irwin, M. J., et al. 2007, *ApJ*, 658, 337  
 Bonaca, A., Hogg, D. W., Price-Whelan, A. M., & Conroy, C. 2019, *ApJ*, 880, 38  
 Bovy, J. 2016, *PhRvL*, 116, 121301  
 Bovy, J., Erkal, D., & Sanders, J. L. 2017, *MNRAS*, 466, 628  
 Caldwell, N., Bonaca, A., Price-Whelan, A. M., Sesar, B., & Walker, M. G. 2020, *AJ*, 159, 287  
 Carlberg, R. G. 2009, *ApJ*, 705, L223  
 Cleveland, W. S., & Devlin, S. J. 1988, *J. Am. Stat. Assoc.*, 83, 596  
 Cohen, J. G., Sesar, B., Bahnholzer, S., et al. 2017, *ApJ*, 849, 150  
 Conroy, C., Bonaca, A., Cargile, P., et al. 2019, *ApJ*, 883, 107  
 Conroy, C., Naidu, R. P., Garavito-Camargo, N., et al. 2021, *Natur*, 592, 534  
 Cunningham, E. C., Deason, A. J., Sanderson, R. E., et al. 2019, *ApJ*, 879, 120

Cunningham, E. C., Garavito-Camargo, N., Deason, A. J., et al. 2020, *ApJ*, 898, 4  
 Dalton, G., Trager, S. C., Abrams, D. C., et al. 2012, *Proc. SPIE*, 8446, 84460P  
 de Boer, T. J. L., Erkal, D., & Gieles, M. 2020, *MNRAS*, 494, 5315  
 De Jong, R. S., Agertz, O., Berbel, A. A., et al. 2019, *Msngr*, 175, 3  
 Deason, A. J., Belokurov, V., Evans, N. W., et al. 2012, *MNRAS*, 425, 2840  
 Deason, A. J., Wetzel, A. R., Garrison-Kimmel, S., & Belokurov, V. 2015, *MNRAS*, 453, 3568  
 DESI, C., Aghamousa, A., Aguilar, J., et al. 2016, arXiv:1611.00036  
 Erkal, D., & Belokurov, V. 2015a, *MNRAS*, 450, 1136  
 Erkal, D., & Belokurov, V. 2015b, *MNRAS*, 454, 3542  
 Erkal, D., Belokurov, V., Bovy, J., & Sanders, J. L. 2016, *MNRAS*, 463, 102  
 Erkal, D., Belokurov, V., Laporte, C., et al. 2019, *MNRAS*, 487, 2685  
 Gaia, C., Brown, A., Vallenari, A., et al. 2018, *A&A*, 616, A1  
 Gaia Collaboration, Prusti, T., de Bruijne, J., et al. 2016, *A&A*, 595, A1  
 Garavito-Camargo, N., Besla, G., Laporte, C. F., et al. 2019, *ApJ*, 884, 51  
 Garavito-Camargo, N., Besla, G., Laporte, C. F., et al. 2021, *ApJ*, 919, 109  
 Garrison-Kimmel, S., Hopkins, P. F., Wetzel, A., et al. 2018, *MNRAS*, 481, 4133  
 Garrison-Kimmel, S., Wetzel, A., Bullock, J. S., et al. 2017, *MNRAS*, 471, 1709  
 Green, S. B., van den Bosch, F. C., & Jiang, F. 2021, *MNRAS*, 503, 4075  
 Grillmair, C. J. 2006, *ApJL*, 645, L37  
 Grillmair, C. J. 2009, *ApJ*, 693, 1118  
 Grillmair, C. J. 2017, *ApJ*, 834, 98  
 Grillmair, C. J., & Dionatos, O. 2006, *ApJL*, 643, L17  
 Harris, C. R., Millman, K. J., van der Walt, S. J., et al. 2020, *Natur*, 585, 357  
 Hopkins, P. F. 2015, *MNRAS*, 450, 53  
 Hopkins, P. F., Wetzel, A., Kereš, D., et al. 2018, *MNRAS*, 480, 800  
 Horta, D., Cunningham, E. C., Sanderson, R. E., et al. 2023, *ApJ*, 943, 158  
 Huber, P. J. 1973, *AnSta*, 1, 799  
 Hunter, J. D. 2007, *CSE*, 9, 90  
 Ibata, R., Malhan, K., Martin, N., et al. 2021, *ApJ*, 914, 123  
 Ivezić, Ž., Kahn, S. M., Tyson, J. A., et al. 2019, *ApJ*, 873, 111  
 Johnston, K. V., Spergel, D. N., & Haydn, C. 2002, *ApJ*, 570, 656  
 Kallivayalil, N., van der Marel, R. P., Alcock, C., et al. 2006, *ApJ*, 638, 772  
 Kazantzidis, S., Bullock, J. S., Zentner, A. R., Kravtsov, A. V., & Moustakas, L. A. 2008, *ApJ*, 688, 254  
 Kim, S. Y., Peter, A. H. G., & Hargis, J. R. 2018, *PhRvL*, 121, 211302  
 Koposov, S. E., Belokurov, V., Li, T. S., et al. 2019, *MNRAS*, 485, 4726  
 Koposov, S. E., Erkal, D., Li, T. S., et al. 2023, *MNRAS*, 521, 4936  
 Law, D. R., Johnston, K. V., & Majewski, S. R. 2005, *ApJ*, 619, 807  
 Leitherer, C., Schaerer, D., Goldader, J. D., et al. 1999, *ApJS*, 123, 3  
 Li, H., Hammer, F., Babusiaux, C., et al. 2021a, *ApJ*, 916, 8  
 Li, T. S., Koposov, S. E., Erkal, D., et al. 2021b, *ApJ*, 911, 149

- Libeskind, N. I., Knebe, A., Hoffman, Y., et al. 2011, *MNRAS*, **411**, 1525
- Lilleengen, S., Petersen, M. S., Erkal, D., et al. 2023, *MNRAS*, **518**, 774
- Lowing, B., Jenkins, A., Eke, V., & Frenk, C. 2011, *MNRAS*, **416**, 2697
- MacQueen, J. 1967, in Berkeley Symp. Math. Statist. Probability 5 (Berkeley, CA: Univ. California Press), 281
- Malhan, K., & Ibata, R. A. 2018, *MNRAS*, **477**, 4063
- Malhan, K., Ibata, R. A., Carlberg, R. G., Valluri, M., & Freese, K. 2019, *ApJ*, **881**, 106
- Malhan, K., Valluri, M., & Freese, K. 2021, *MNRAS*, **501**, 179
- Mateu, C. 2023, *MNRAS*, **520**, 5225
- McMillan, P. J. 2017, *MNRAS*, **465**, 76
- Myeong, G. C., Jerjen, H., Mackey, D., & Da Costa, G. S. 2017, *ApJL*, **840**, L25
- Nadler, E. O., Banerjee, A., Adhikari, S., Mao, Y.-Y., & Wechsler, R. H. 2021, *ApJL*, **920**, L11
- Nadler, E. O., Wechsler, R. H., Bechtol, K., et al. 2020, *ApJ*, **893**, 48
- Panithanpaisal, N., Sanderson, R. E., Wetzel, A., et al. 2021, *ApJ*, **920**, 10
- Pawlowski, M. S., & Kroupa, P. 2020, *MNRAS*, **491**, 3042
- Pearson, S., Clark, S. E., Demirjian, A. J., et al. 2022, *ApJ*, **926**, 166
- Peñarrubia, J., Gomez, F. A., Besla, G., Erkal, D., & Ma, Y.-Z. 2016, *MNRAS: Letters*, **456**, L54
- Perez, F., & Granger, B. E. 2007, *CSE*, **9**, 21
- Petersen, M. S., & Peñarrubia, J. 2020, *MNRAS: Letters*, **494**, L11
- Petersen, M. S., Weinberg, M. D., & Katz, N. 2022, *MNRAS*, **510**, 6201
- Pietrzynski, G., Graczyk, D., Gallenne, A., et al. 2019, *Natur*, **567**, 200
- Planck Collaboration, Ade, P., Aghanim, N., et al. 2016, *A&A*, **594**, A13
- Power, C., Navarro, J. F., Jenkins, A., et al. 2003, *MNRAS*, **338**, 14
- Price-Whelan, A. M., & Bonaca, A. 2018, *ApJL*, **863**, L20
- Robles, V. H., Kelley, T., Bullock, J. S., & Kaplinghat, M. 2019, *MNRAS*, **490**, 2117
- Sales, L. V., Navarro, J. F., Kallivayalil, N., & Frenk, C. S. 2017, *MNRAS*, **465**, 1879
- Salomon, J.-B., Libeskind, N., & Hoffman, Y. 2023, *MNRAS*, **523**, 2759
- Samuel, J., Wetzel, A., Chapman, S., et al. 2021, *MNRAS*, **504**, 1379
- Samuel, J., Wetzel, A., Tollerud, E., et al. 2020, *MNRAS*, **491**, 1471
- Sanders, J. L., Bovy, J., & Erkal, D. 2016, *MNRAS*, **457**, 3817
- Sanders, J. L., Lilley, E. J., Vasiliev, E., Evans, N. W., & Erkal, D. 2020, *MNRAS*, **499**, 4793
- Sanderson, R. E., Wetzel, A., Loebman, S., et al. 2020, *ApJS*, **246**, 6
- Santistevan, I. B., Wetzel, A., Tollerud, E., et al. 2024, *MNRAS*, **527**, 8841
- Savino, A., Weisz, D. R., Skillman, E. D., et al. 2022, *ApJ*, **938**, 101
- Shapiro, S. S., & Wilk, M. B. 1965, *Biometrika*, **52**, 591
- Spergel, D., Gehrels, N., Baltay, C., et al. 2015, arXiv:1503.03757
- Spergel, D., Gehrels, N., Breckinridge, J., et al. 2013, arXiv:1305.5422
- Takada, M., Ellis, R. S., Chiba, M., et al. 2014, *PASJ*, **66**, R1
- van den Bosch, F. C., Ogiya, G., Hahn, O., & Burkert, A. 2018, *MNRAS*, **474**, 3043
- van der Velden, E. 2020, *JOSS*, **5**, 2004
- Vasiliev, E. 2019, *MNRAS*, **482**, 1525
- Vasiliev, E. 2023, *Galax*, **11**, 59
- Vasiliev, E. 2024, *MNRAS*, **527**, 437
- Vasiliev, E., Belokurov, V., & Erkal, D. 2021, *MNRAS*, **501**, 2279
- Virtanen, P., Gommers, R., Oliphant, T. E., et al. 2020, *NatMe*, **17**, 261
- Vogelsberger, M., Zavala, J., & Loeb, A. 2012, *MNRAS*, **423**, 3740
- Weinberg, M. D. 2023, *MNRAS*, **525**, 4962
- McKinney, W. 2010, in Proc. of the 9th Python in Science Conf., ed. S. van der Walt & J. Millman, 61
- Wetzel, A., & Garrison-Kimmel, S. 2020a, GizmoAnalysis: Read and Analyze Gizmo Simulations, Astrophysics Source Code Library, ascl:2002.015
- Wetzel, A., & Garrison-Kimmel, S. 2020b, HaloAnalysis: Read and Analyze Halo Catalogs and Merger Trees, Astrophysics Source Code Library, ascl:2002.014
- Wetzel, A., Hayward, C. C., Sanderson, R. E., et al. 2023, *ApJS*, **265**, 44
- Wetzel, A. R., Deason, A. J., & Garrison-Kimmel, S. 2015, *ApJ*, **807**, 49
- Wetzel, A. R., Hopkins, P. F., Kim, J.-h., et al. 2016, *ApJL*, **827**, L23
- Wilks, S. S. 1938, *Psychometrika*, **3**, 23
- Williams, M. E. K., Steinmetz, M., Sharma, S., et al. 2011, *ApJ*, **728**, 102
- Yam, W., Carlin, J. L., Newberg, H. J., et al. 2013, *ApJ*, **776**, 133
- Yoon, J. H., Johnston, K. V., & Hogg, D. W. 2011, *ApJ*, **731**, 58
- Zonca, A., Singer, L., Lenz, D., et al. 2019, *JOSS*, **4**, 1298